Direct Strength Method for the Flexural Design of Through-Fastened Metal Building Roof and Wall Systems under Wind Uplift or Suction

Tian Gao

Dissertation submitted to the faculty of the Virginia Polytechnic Institute and State University in partial fulfillment of the requirements for the degree of

Doctor of Philosophy
In
Civil Engineering

Cristopher D. Moen, Committee Chair
W. Samuel Easterling
Thomas E. Cousins
William J. Wright

3 August 2012
Blacksburg, VA

Keywords: Through-Fastened, Metal Building, Purlin, Uplift Loading, Rigid Insulation.

Direct Strength Method for the Flexural Design of Through-Fastened Metal Building Roof and Wall Systems under Wind Uplift or Suction

Tian Gao

Abstract

The design of metal building roof and wall systems under uplift and suction wind loading is complicated because the laterally unbraced purlin and girt's free flange is compressed, and the cross-section rotates due to the shear flow. The objective of this thesis is to introduce a Direct Strength Method (DSM) prediction approach for simple span purlins and girts with one flange through-fastened under uplift or suction loading. This prediction method is also applicable for the case when rigid board insulation is placed between the metal panel and through-fastened flange. The prediction method is validated with a database of 62 simple span tests. To evaluate the prediction for the case when rigid board is used, 50 full-scale tests with rigid board insulation are conducted by the author of this thesis. In the experimental study panel failure, connection failure and member (purlin and girt) failure are observed, and they all limit the system's capacity. Another important contribution of this thesis is that it builds the foundation for future study of a general, mechanics-based limit state design approach for metal building roof and wall systems that can accommodate uplift and gravity loads, simple and continuous spans, and through-fastened and standing seam roofs.

Acknowledgements

So many thanks to the people in my life in the past three years. My wife Yimeng always supports me no matter if I am wrong or not. I know she is just trying to make me feel better. On a lot things, she totally disagrees with me! But, the confidence she delivered is very important to me. Thanks for her understanding and tolerance. Thanks for all supporting from my parents Wenjie and Dongzhi and my parents in low Linghua and Qiang. They may not see I put their names here, but I will definitely let them know.

I had a really enjoyable three-year Ph.D. life with my advisor Dr. Cris Moen. People may not believe that Ph.D. life can be enjoyable. I didn't believe it either until today, but it happens to me. I really appreciate Dr. Moen's tolerance to my wrong English grammars, typing errors, poor writing and repeating them again, again and again. Dr. Moen gives me a lot of freedom and trust. He always encourages me and stands on the same side with me. People think Ph.D. is a tough process, but it is not to me. My Ph.D. study is basically doing whatever I want to do, plus knowing some good friends. After I graduate, hopefully he can find another one to give him a ride at 2:00am in the morning.

I also thank my committee members, Dr. W. Samuel Easterling, Dr. Thomas Cousins and Dr. William Wright for their help and valuable advises. I really appreciate the opportunity given by Dr. Easterting and Dr. Cousins three years ago to accept me, a Wood Science background student, as a Civil Engineering Ph.D. student. I will also thank Dr. Matthew Eatherton for the TA opportunity. Sorry, I was not that helpful though.

I will also thank Dr. Lee Shoemaker, Mr. Dan Walker and Mr. Jerry Hatch from Metal Building Manufactures Association for the funding support and the excellent advices from an industrial standing point.

Thank all my Lab friends, David, Brett and Dennis. I cannot finish 50 full-scale "double-crane" Vacuum box tests without your help and support. Thank all my research group friends, David (Padilla), Tao, Big Ryan, Cojo, Chris, Luck, Matt, Paul, Galo, Adrian et al. Thank all you guys' hanging out with me in the Lab. And also, Marc, a wonderful listener.

The three-month study in Johns Hopkins University is a super important start to my whole thesis. I really appreciate Dr. Ben Shafer's help and my friends in Johns Hopkins, especially Zhanjie, Luiz and Nick.

Thanks BCF Church, where I can find the peace every Sunday morning!

Life is a tough (--Nick, JHU) but exciting (--Zhe, former roommate) adventure (--Dr. Moen)! Let's enjoy it!

Table of Contents

List of Figures

List of Tables

Chapter 1: Introduction

1.1 Objective and motivation

The design of metal building roof and wall systems is complicated because of the diversity of design variables, e.g., different purlin and girt cross-sections, simple or continuous span, through-fastened roof (wall) or standing seam roof, with or without insulation, and uplift (suction) or gravity (pressure) loadings. The overall objective of this thesis is to lay the groundwork for a new strength prediction approach that extends the American Iron and Steel Institute's Direct Strength Method (DSM) to all types of metal building wall and roof systems. The specific focus of the research presented herein is through-fastened simple span purlins or girts with the laterally unbraced free flange in compression caused by wind suction on a wall or wind uplift on a roof. A detailed description of this system behavior is provided in the following section.

1.2 System behavior

Under a uplift (suction) loading (Fig. 1.1a), the bending moments and stresses in a girt or purlin at Section-*B* in Fig. 1.1b are greater than the one at the Section-*A*, A part of flange is assumed to be cut at the edge-*E* parallel to the free edge. The direction of the shear stress τ on the edge-*E* is from edge-*B* to edge-*A*, because σ_B is greater than σ_A. The stress τ at the edge-*E* is caused by the difference of the axial stresses σ_B and σ_A calculated based on the difference in the bending moment (ΔM). Because ΔM decreases as a function of x, the stress τ decreases as a function of x, i.e., τ_A is greater than τ_B. So the shear stress on the edge-*A* is greater than the one on the edge-*B*, and the total force w on the cut piece is from the free edge to the edge-*E*. Using the same concept, the shear flow direction is determined as shown in Fig. 1.1(c) for a Z- and C-section.

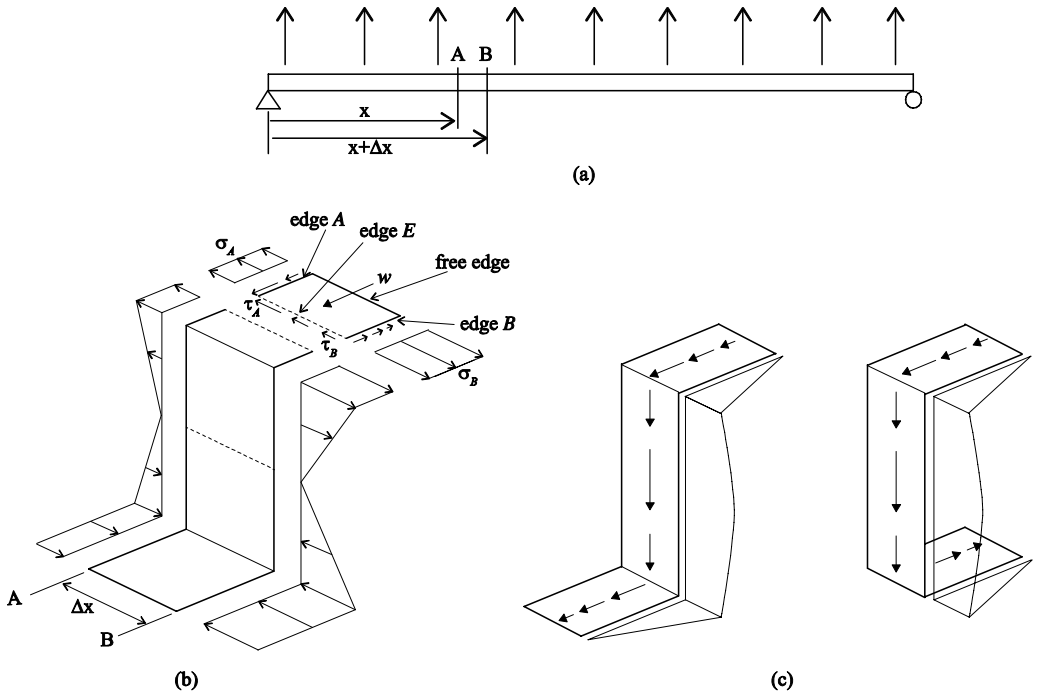

Fig. 1.1 (a) Uplift loading (b) shear stress (c) shear flow

The shear flow causes the cross-section to rotate (see Fig. 1.2), and combines with lateral-torsional buckling deformation at failure. The through-fastened sheathing provides rotational restraint to the purlin or girt at the through-fastened flange when the cross-section rotates. New mechanics-based rotational restraint equations are derived and validated in Chapter 2 of this thesis based on the panel pull-out stiffness at the screw and the through-fastened flange bending. When rigid board foam insulation is present between the through fastened flange and panel (see Fig. 1.3), the rotational restraint changes, and this is another focus of this thesis. The rotational restraint for the case when rigid board insulation is present is dealt with in Chapter 5 using a simplified method.

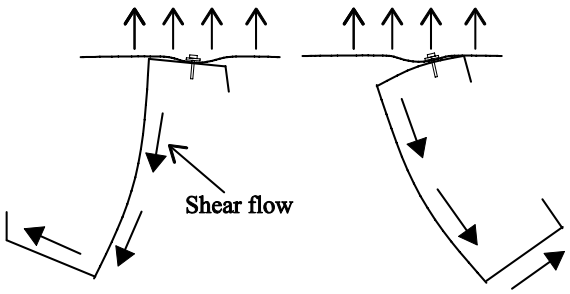

Fig. 1.2 Cross-section rotation caused by the shear flow with bare panel

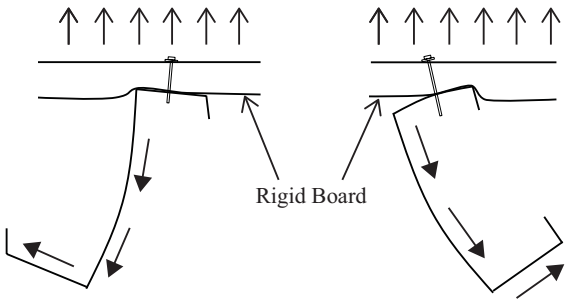

Fig. 1.3 Cross-section rotation caused by the shear flow with rigid board

1.3 Existing design methods

R-factor method

The R-factor method is used to predict through-fastened girt and purlin flexural capacity in North America (AISI), Australia and New Zealand (AS/NZS), where $M_n=RS_eF_y$. The R-factor is calculated as $R=M_{test}/S_eF_y$, where M_{test} is the tested roof or wall system capacity using a vacuum box test [1], S_e is the purlin or girt effective section modulus, and F_y is the purlin or girt yield stress. However, this R-factor is only applicable to roof and wall systems that have been tested, i.e., the system variables such as panel profile, fastener size, purlin or girt local slenderness, and span length have to be within the tested limits. To use a new system for variables falling outside these dimensional limits, more tests are required. For example using rigid board insulation in a metal building wall system is highly recommended by the energy code, e.g., ASHRAE-90.1 2010 [2], however, the R-factor for this new type of rigid board-insulated system

does not exist in the design specifications, and so vacuum tests are needed to determine the new R-factors. In the Chapter 3 of this thesis, wall systems with different girt cross-section and the rigid insulation thicknesses are tested and the R-factors for the wall system with the rigid board insulation is determined.

Eurocode method (EN-1993)

In the Eurocode flexural strength prediction method for through-fastened roof and wall systems, a semi-analytical approach is used to predict the through-fastened purlin and girts capacity. The purlin or girt failure stress is determined as:

$$\frac{1}{\chi_{LT}} \cdot \frac{M_x}{S_e} + \sigma_f \leq F_y \qquad (1.1)$$

The first term in the left of Eq. (1.1) is the stress due to the lateral-torsional buckling deformation. The moment M_x is the required purlin or girt moment capacity and χ_{LT} is the reduction factor for lateral-torsional buckling deformation including the effect of rotational restraint, and calculated using European buckling curve-b. The stress σ_f is from lateral deformation of the free flange caused by shear flow. The detailed calculation of σ_f is presented in Chapter 4 of this thesis. The rotational restraint provided by the sheathing to the purlin or girt is needed in the calculation of σ_f, and it can only be quantified by a rotational restraint test, also known as an F-test [3]. The inconvenience of obtaining the rotational restraint limits the implementation of the Eurocode method. Also, the center of twist for the Z-section used in the Eurocode is not consistent with experimental observations. The Chapter 4 of this thesis shows that modifying the assumed center of twist location for the Z-section can improve the accuracy of the Eurocode prediction.

1.4 Direct Strength Method (DSM)

DSM [4] is a relatively new method to calculate the beam and column capacity with member's elastic local, distortional and global buckling loads, i.e. $M_{cr\ell}$, M_{crd} and M_{cre} for beams ($P_{cr\ell}$, P_{crd} and P_{cre} for columns) using empirical equations. Local buckling is thin plate buckling of individual slender elements (web, flange and stiffener), where the intersection of elements do not move. Distortional buckling is only for open cross-sections, where the compressed flanges buckle (the intersection of the compressed flange and the stiffener moves). Global buckling is also known as Euler buckling (lateral-torsional buckling in beams). The critical elastic buckling loads can be calculated with eigen-buckling analysis using the finite strip method, and in this thesis, the freely available program CUFSM [5] is employed as shown in Fig. 1.4.

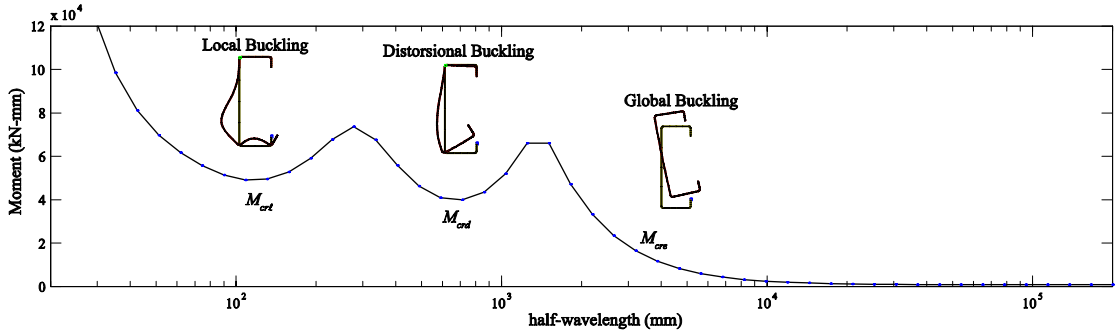

Fig. 1.4 Elastic buckling loads in CUFSM

The flexural strength is determined as M_n=min (M_{ne}, $M_{n\ell}$, M_{nd}). The global buckling capacity M_{ne} is calculated as:

$$\begin{aligned} M_{ne} &= M_{cre} \quad For \quad (M_{cre} < 0.56M_y) \\ M_{ne} &= \frac{10}{9}M_y\left(1-\frac{10M_y}{36M_{cre}}\right) \quad For \quad (2.78M_y \geq M_{cre} \geq 0.56M_y) \\ M_{ne} &= M_y \quad For \quad (M_{ne} > 2.78M_y) \end{aligned} \tag{1.2}$$

where $M_y=S_fF_y$, and S_y is the gross-section modulus. The local-global buckling interaction capacity $M_{n\ell}$ is calculated as:

$$\begin{aligned} M_{n\ell} &= M_{ne} \quad For \quad (\lambda_\ell \le 0.776) \\ M_{n\ell} &= \left(1-0.15\left(\frac{M_{cr\ell}}{M_{ne}}\right)^{0.4}\right)\left(\frac{M_{cr\ell}}{M_{ne}}\right)^{0.4} M_{ne} \quad For \quad (\lambda_\ell > 0.776) \end{aligned} \tag{1.3}$$

where $\lambda_\ell=(M_{ne}/M_{cr\ell})^{0.5}$, and M_{ne} is obtained from Eqs. 1.3. The distortional buckling capacity M_{nd} is calculated as:

$$\begin{aligned} M_{nd} &= M_y \quad For \quad (\lambda_d \le 0.673) \\ M_{nd} &= \left(1-0.22\left(\frac{M_{crd}}{M_y}\right)^{0.5}\right)\left(\frac{M_{crd}}{M_y}\right)^{0.5} M_y \quad For \quad (\lambda_d > 0.673) \end{aligned} \tag{1.4}$$

where $\lambda_d=(M_y/M_{crd})^{0.5}$.

DSM is currently being used primarily to calculate the capacity of beam and column components, but in this thesis the approach will be extended to calculate purlin and girt in the roof and wall systems.

1.5 DSM for the purlin and girt design

To calculate through-fastened purlin or girt system strength, a protocol for including the rotation effect caused by shear flow and the rotational restraint is needed for DSM. In the Chapter 4, this protocol is implemented as a knock down factor to account for the shear flow effect, and a rotational spring is applied in CUFSM to calculate the critical buckling loads including the restraint from the sheathing.

1.6 Experimental study for the system with rigid board insulation

Vacuum box tests were conducted as a part of this thesis to evaluate the proposed DSM prediction method for the case when the rigid board insulation is present.. During

the study, different failure modes (wall panel flexural failure, connection failure and girt failure) were observed. However, the existing prediction methods, i.e., the R-factor method and Eurocode method, as well as the proposed DSM method, are only applicable to purlin or girt flexural strength. Therefore, this thesis concludes with a proposal for important future study addressing limit state design of metal building roof and wall systems considering the through-fastened panel and connection strength.

1.7 Thesis outline and research progression

Since the rotational restraint provided by the roof and wall sheathing plays an important role in the calculation of the flexural capacity of the through-fastened purlin and girt, the research starts in Chapter 2 with a development of a mechanical model to calculate the rotational restraint provided by the through-fastened bare metal panels. The calculation is validated with rotational restraint tests conducted by the author of this thesis at John Hopkins University. In Chapter 3, full-scale wall systems with or without rigid board insulation are tested. Four different failure modes limiting the system capacity are observed during the study. These observations identify future work regarding a limit state design of metal building roof and wall systems that are listed in Chapter 6. In Chapter 4, the calculation of rotational restraint developed in Chapter 2 is applied with the Eurocode and DSM methods for predicting simple span through-fastened purlin or girt flexural capacity when the compressed flange is unbraced. The Eurocode, DSM and the experimentally derived R-factor methods are evaluated with a database of 62 simple span tests assembled by the author of this thesis. The result shows that the Eurocode method can be improved with minor modifications and the R-factor method is accurate for C-sections but unconservative for Z-section. The DSM prediction is confirmed to be

viable and accurate for simple spans. Chapter 5 is focused on the prediction of the flexural capacity of girts through-fastened to the wall system with rigid board insulation. A simplified model is developed to calculate the rotational restraint provided by the wall system with the rigid board insulation sandwiched between the girt and bare panel, and similar to Chapter 2 the calculation is evaluated with F-tests. The rotational restraint calculation is then applied into the methods described in Chapter 4 to predict the flexural capacity of girts. The results are discussed and evaluated with the vacuum box tests conducted in Chapter 3. Chapter 6 highlights and summarizes the important conclusions from this research and provides a comprehensive list of ideas for future work.

References

[1] Fisher JM. Uplift Capacity of Simple Span Cee and Zee Members with Through-Fastened Roof Panels". Report for Metal Building Manufacturers Association, Cleveland, OH; 1996.

[2] ASHRAE-90.1. ASHRAE Standard: Energy Standard for Buildings Except Low-Rise Residential Buildings. American Society of Heating, Refrigerating and Air-Conditioning Engineers, Inc., Atlanta, GA; 2010.

[3] LaBoube RA. Roof panel to purlin connections: rotational restraint factor. In: IABSE Colloquium on Thin-Walled Metal Structures in Buildings. Stockholm, Sweden; 1986.

[4] AISI-S100. North American Specification for the Design of Cold-Formed Steel Structural Members. Washington, D.C.: American Iron and Steel Institute, 2007.

[5] Schafer BW. Adany, S. Buckling Analysis of Cold-formed Steel Members Using CUFSM: Conventional and Constrained Finite Strip Methods. Proc., 18th International Specialty Conference on Cold-Formed Steel Structures, Orlando, FL; 2006.

Chapter 2: Prediction of Rotational Restraint Provided by Through-Fastened Connections in Metal Building Roof and Wall Systems

*(*To appear in *Thin-walled Structures)*

"Prediction of Rotational Restraint Provided by Through-Fastened Connections in Metal Building Roof and Wall Systems"

Abstract

This paper introduces mechanics-based expressions for predicting the rotational restraint provided by through-fastened metal panels to Z- and C-section girts or purlins. The analytical prediction equations include the effect of local panel deformation at a screw and girt or purlin flange bending at a through-fastened connection. Finite element parameter studies are performed to quantify the local fastener pull-out stiffness for a common panel profile, and flange bending stiffness is determined with a cantilever beam model. Rotational restraint experiments are conducted to validate the prediction equations. The through-fastened connection stiffness is simulated in a finite strip elastic buckling analysis with a rotational spring to demonstrate how system effects can be included in design.

2.1 Introduction

A common pre-manufactured metal building construction method is to through-fasten exterior steel panels to the flat flanges of cold-formed steel wall girts and roof purlins with screws as shown in Fig. 2.1 [1]. The wall and roof are designed to resist suction (uplift) from wind that places the unbraced C- or Z-section flange in compression, resulting in lateral-torsional buckling deformation. Additional lateral bending combines with the buckling deformation in a Z-section because the centroidal strong axis bending moment M_x from the wind pressure acts on the point symmetric cross-section about inclined principal axes (i.e., $M_x=M_1 + M_2$ in vector space, see Fig. 2.1a) [2-4]. For a C-section, additional lateral deformation results from shear flow in the flanges caused by torsion (M_z in Fig. 2.1b) developed by the eccentricity of the fastener line to the C-section

shear center [5]. The girt or purlin is partially restrained against rotation by the through-fastened screw connection. The amount of restraint influences the longitudinal bending and warping torsion stress magnitudes and distribution under load [6-9] and ultimately defines the capacity of the wall or roof system.

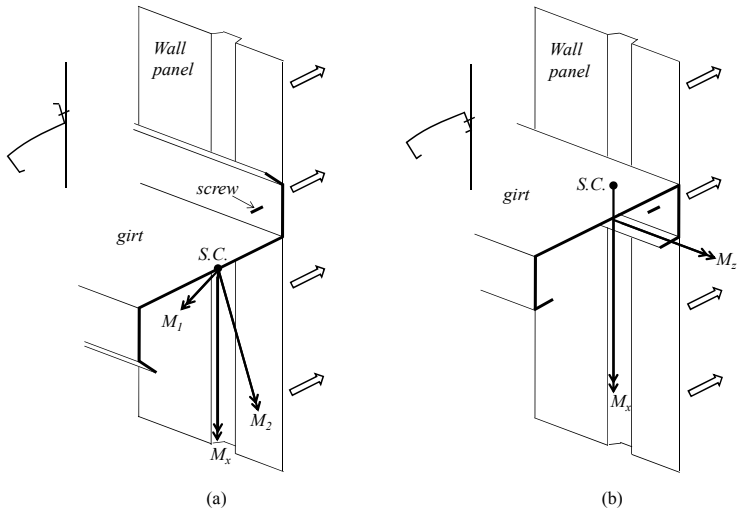

Fig. 2.1 (a) Biaxial bending in a Z-section; (b) torsion in a C-section from the load eccentricity

Previous research by the metal building industry dating back to the early 1970s hypothesized that rotational restraint provided to a through-fastened wall girt and roof purlin is a function of panel thickness and the through-fastened flange width to thickness ratio [10]. The F-test was developed as a way to experimentally quantify the rotational restraint for specific roof and wall systems [11]. Rotational stiffness of the through-fastened connection is measured in an F-test by subjecting a small cantilever segment of metal panel attached to a girt or purlin to a concentrated moment [12]. Experimental programs employing the F-test confirmed that rotational restraint is influenced by local deformation at the screw connection [13-14], i.e., the thicker the base metal thickness of the panel and flange the larger the rotational stiffness.

In this study, engineering expressions for predicting rotational restraint (stiffness) are derived and validated for C- and Z-sections that are through-fastened with screws to metal panels. The equations explicitly include the influence of panel and flange base metal thickness. This mechanics-based prediction of rotational restraint is an important step forward in the implementation of a limit state strength prediction approach for metal building wall and roof systems, a topic of considerable study over the past 20 years [15-26].

A potential application of the rotational restraint equations presented in this paper is to calculate the through-fastened restraint and model the stiffness as a rotational spring at the tension flange of a girt or purlin cross-section in a finite strip elastic buckling analysis program, for example the freely available program CUFSM [26]. In CUFSM, the critical elastic global (lateral-torsional) buckling moment can be calculated including the influence of rotational restraint. The buckling moment is then used with existing American Iron and Steel Institute (AISI) Direct Strength Method (DSM) equations [28, 29] to predict flexural capacity. The tensile force in the screw fasteners can also be calculated with the rotational restraint expressions if the cross-section rotation along the span is available or can be approximated [30]. A detailed derivation of the rotational restraint expressions is provided in the next section, followed by a summary of a rotational restraint (F-test) experimental program that is used to validate the mechanics-based prediction models.

2.2 Rotational restraint prediction

2.2.1 Prediction framework

A mechanics-based model is developed in this section that predicts rotational restraint as a girt or purlin rotates relative to a through-fastened metal panel. It is assumed that the connection restraint, $k_{\phi c}$, with units of force·length/rad/length, can be represented as a set of rotational springs in series

$$k_{\phi c} = \left(\frac{1}{k_{\phi p}} + \frac{1}{k_{\phi f}} \right)^{-1} . \tag{2.1}$$

Cross-section rotation is resisted as the screw pulls and bends the panel, $k_{\phi p}$, and by the bending stiffness of the through-fastened flange, $k_{\phi f}$.

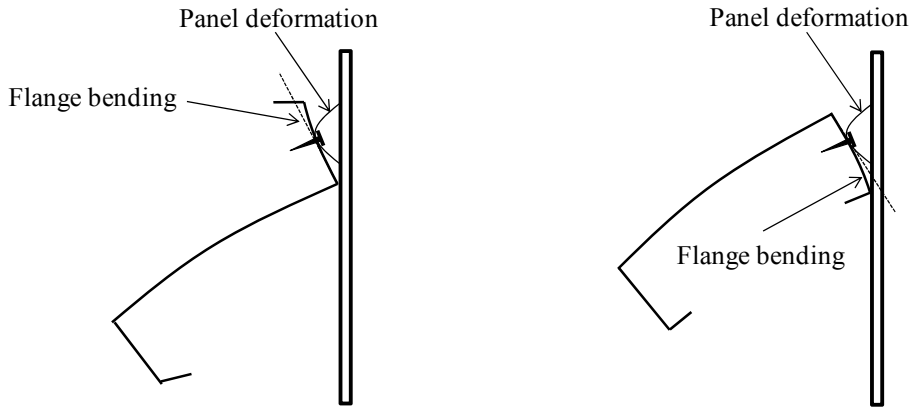

Fig. 2.2 Panel deformation and flange bending in a (a) Z-section; (b) C-section

2.2.2 Influence of metal panel deformation on rotational restraint

The rotational restraint per unit length provided by the metal panel to a through-fastened girt or purlin is approximated as

$$k_{\phi p} = \frac{M}{\theta_p} = \frac{c^2 k_p}{S} \tag{2.2}$$

where M is a moment per unit length calculated as the force to deflect the panel $\delta(k_p/S)$ multiplied by the distance c between the fastener and the flange pivot point as shown in Fig. 2.3. The panel pullout stiffness and deflection at the fastener are k_p (force/length) and δ (length) respectively as shown in Fig. 2.3. Rotational restraint is assumed to be evenly distributed between fasteners and this is why the panel pullout stiffness is calculated as k_p/S, where S is the distance between fasteners. The cross-section rotation θ_p is approximated for small angles as δ/c.

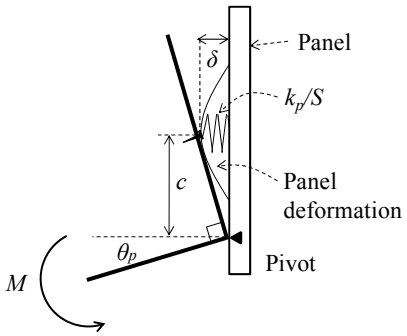

Fig. 2.3 Cross-section (rigid body) rotation due to the panel deformation

2.2.3 Influence of through-fastened flange bending on rotational restraint

Rotational restraint provided by a girt or purlin flange as it is bent by the fastener force depends on the cross-section type (Z or C) as shown in Fig. 2.4. For a Z-section, the through-fastened flange can be treated as a cantilever beam to calculate $k_{\phi f}$ as shown in Fig. 2.4a, resulting in

$$k_{\phi fZ} = \frac{M}{\theta_{fZ}} = \frac{3EI}{cS} \ . \tag{2.3}$$

The distributed moment M is equal to $\delta(k_{fZ}/S)c$, again a spring force multiplied by the moment arm c, where $k_{fZ}=3EI/c^3$ is the flexural stiffness of a cantilever with a point load at its tip assuming that the web-flange corner remains a right angle after rotation occurs. The cross-section rotation θ_{fZ} is approximated for small angles as δ/c. The contributory

girt or purlin flange moment of inertia to one screw fastener is assumed as $I=St_s^3/12$, where t_s is the girt or purlin base metal thickness, and E is the girt or purlin modulus of elasticity. Although the screw spacing S appears in Eq. (2.3), the assumed flange bending restraint $k_{\phi fZ}$ is not a function of screw spacing because I is also a function of S and the two instances cancel out.

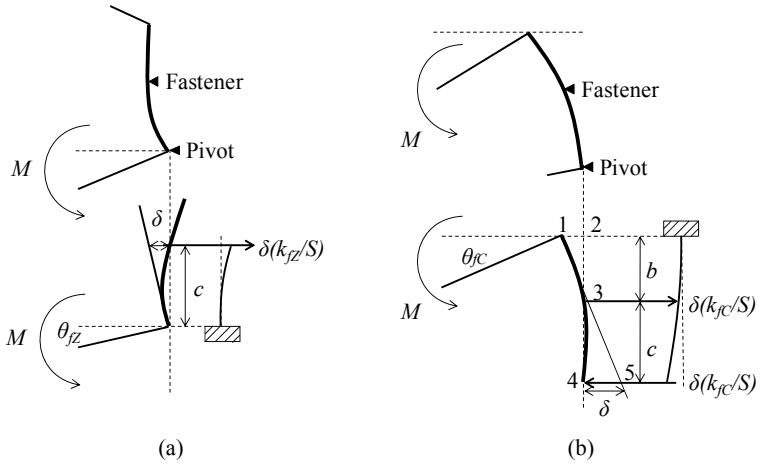

Fig. 2.4 Flange bending model for (a) Z-section; (b) C-section

For a C-section, flange bending restraint $k_{\phi f}$ is calculated assuming the flange acts as a cantilever loaded with a force couple as shown in Fig. 2.4b

$$k_{\phi fC} = \frac{M}{\theta_{fC}} = \frac{c^2 EI}{\left(\frac{b^2 c}{2} + c^2 b + \frac{c^3}{3}\right) S} \quad . \tag{2.4}$$

Consistent with the treatment for a Z-section in Eq. (2.3), the moment M on the panel is equal to $\delta(k_{fC}/S)c$ and the cross-section rotation θ_{fC} is approximated for small angles as δ/c. The calculation of k_{fC} at the free end (point-4 in Fig 2.4b) using the cantilever analogy is calculated with the second moment area theorem assuming 132= 435 in Fig.2.4b, where the line-15 is perpendicular to the web, and point-3 is the intersection of the line-24 and line-15, resulting in

$$k_{fC} = \frac{EI}{\frac{b^2 c}{2} + c^2 b + \frac{c^3}{3}} \tag{2.5}$$

where b is the distance between the flange-web corner and fastener in the C-section. Note that $k_{\phi fC}$ in Eq. (2.5) is not a function of screw spacing because I is also a function of S.

Substituting Eq. (2.2) and Eq. (2.3) into Eq. (2.1) leads to the distributed rotational stiffness along a through-fastened Z-section flange

$$k_{\phi cZ} = \left(\frac{S}{c^2 k_p} + \frac{cS}{3EI} \right)^{-1}. \tag{2.6}$$

For a C-section, the distributed rotational stiffness is obtained by substituting Eqs. (2.2) and (2.4) into Eq. (2.1)

$$k_{\phi cC} = \left(\frac{S}{c^2 k_p} + \frac{\left(\frac{b^2 c}{2} + c^2 b + \frac{c^3}{3} \right) S}{c^2 EI} \right)^{-1}. \tag{2.7}$$

A method for calculating the panel stiffness k_p is presented in the next section, followed by a validation study where Eq. (2.6) and Eq. (2.7) are compared to experimental data from rotational restraint tests.

2.2.4 Calculating metal panel stiffness at the screw location with finite element analysis

Metal panel stiffness k_p is calculated with thin shell second order elastic finite element analysis in ABAQUS [31] (*STATIC with NLGEOM turned on) for a typical metal panel profile in Fig. 5 assuming the modulus of elasticity E=205 GPa. The panel is fixed at its base and the corner bearing pivot point of a girt or purlin stretching along the panel (consistent with an F-test) is simulated by restraining the out-of-plane translational

degrees of freedom (Fig. 2.6). A point load of increasing magnitude is applied to simulate the fastener pull-out force, and the deflection at the location of the point load is recorded. The load-deformation response is nonlinear - initially with a low stiffness dominated by flexure and then converging towards a constant higher stiffness as membrane action engages for large deformations [32, 33]. The converged membrane dominated stiffness is chosen as k_p at approximately δ/t_w=5, where t_w is the wall panel thickness.

The panel stiffness, k_p, varies both with the screw placement relative to the ribs and with the location of the fastener relative to the cross-section pivot point, i.e., the distance c. The panel stiffness is provided in Figs. 7-9 for three different fastener-to-rib locations and two common panel thicknesses - 24 gauge (t_w=0.56 mm) and 26 gauge (t_w=0.46 mm), as a function of screw location in the flange, c.

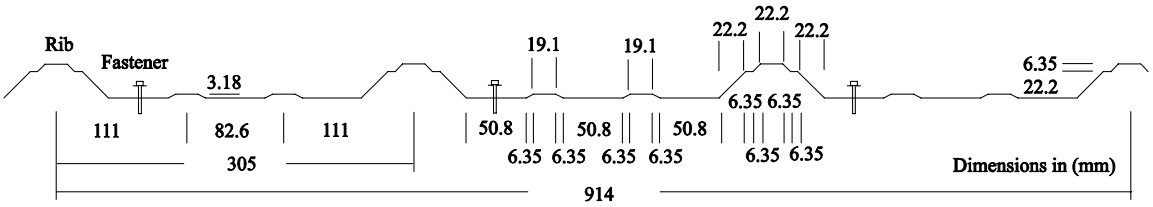

Fig. 2.5 Panel cross-section and fastener location

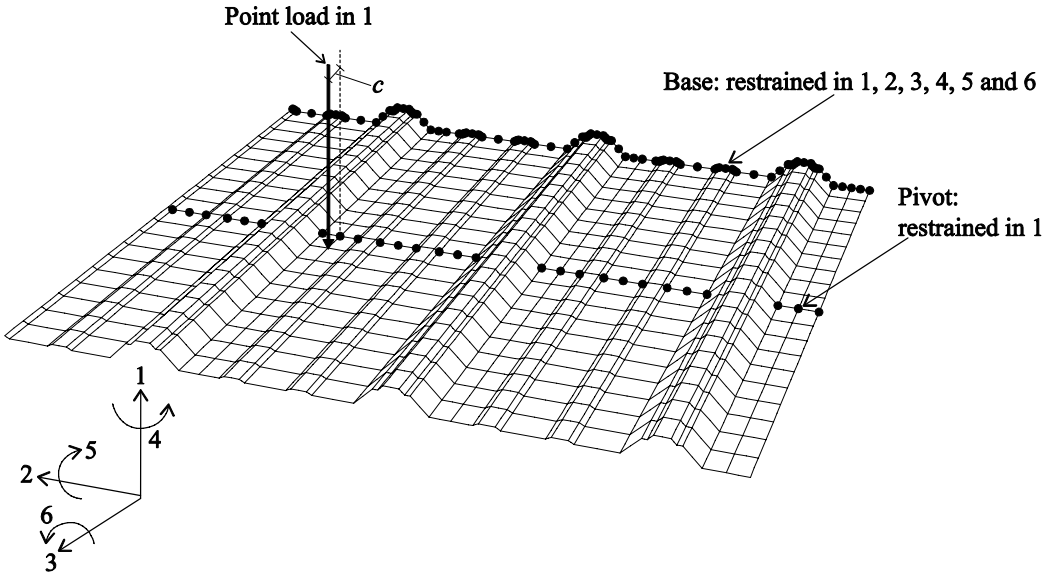

Fig. 2.6 Metal panel loading and boundary conditions in ABAQUS

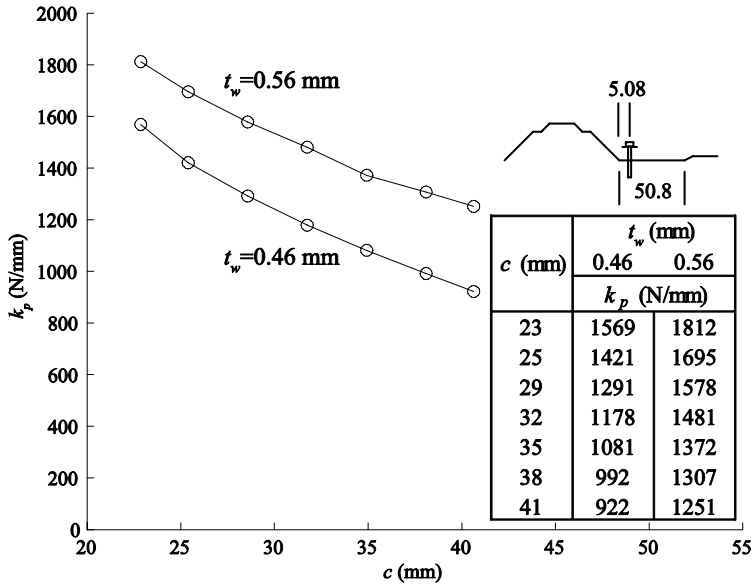

c (mm)	t_w (mm) 0.46	0.56
	k_p (N/mm)	
23	1569	1812
25	1421	1695
29	1291	1578
32	1178	1481
35	1081	1372
38	992	1307
41	922	1251

Fig. 2.7 Panel stiffness k_p for the fastener-to-rib distance of 5.08mm

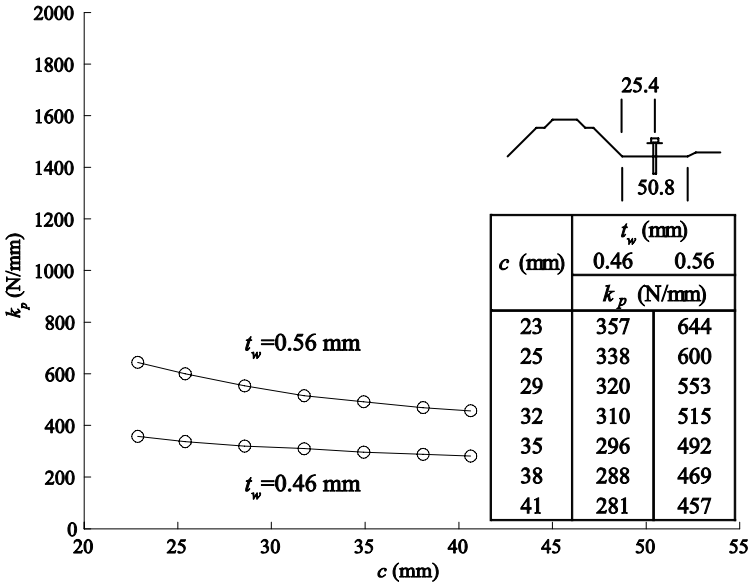

c (mm)	t_w (mm) 0.46	0.56
	k_p (N/mm)	
23	357	644
25	338	600
29	320	553
32	310	515
35	296	492
38	288	469
41	281	457

Fig. 2.8 Panel stiffness k_p for the fastener-to-rib distance of 25.4mm

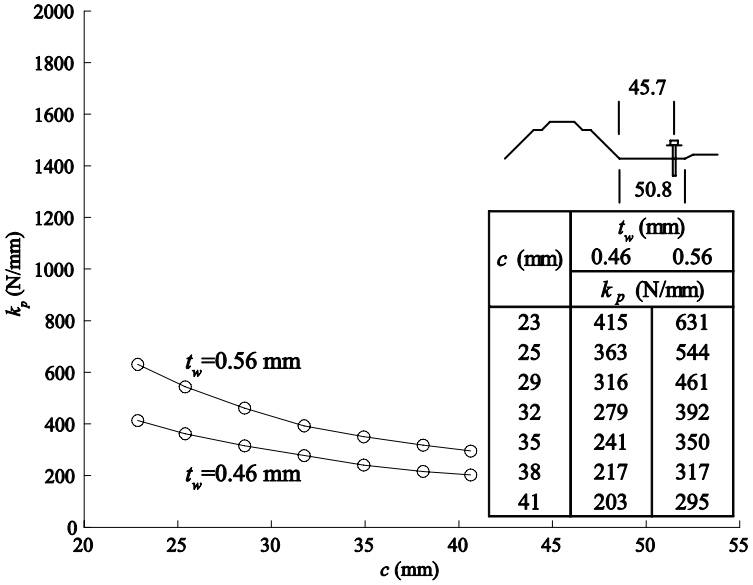

c (mm)	t_w (mm) 0.46	0.56
	k_p (N/mm)	
23	415	631
25	363	544
29	316	461
32	279	392
35	241	350
38	217	317
41	203	295

Fig. 2.9 Panel stiffness k_p for the fastener-to-rib distance of 45.7mm

2.3 Experimental validation

2.3.1 Testing strategy and cross-section dimensions

To evaluate the accuracy of Eq. (2.6) and Eq. (2.7), rotational restraint tests were conducted on C- and Z-section cold-formed steel members through-fastened to a metal panel. Five cross-section types were studied to explore the influence of flange bending on

through-fastened rotational stiffness. The specimen names, measured cross-section dimensions, and measured base metal thicknesses are summarized in Table 2.1. The dimension notations are shown in Fig. 2.10. The screw location in the flange, i.e., *b* and *c*, were carefully measured at each fastened location in a specimen. The average *b* and *c* are provided in Table 2.1, and the coefficient of variation (COV) within each specimen ranged from 0.03 to 0.12. The stiffener, *d*, is approximately 25 mm, and the stiffener angle, γ, is approximately 50^o and 90^o for Z- and C-section respectively. The inside corner radius, *R*, is approximately 4 mm.

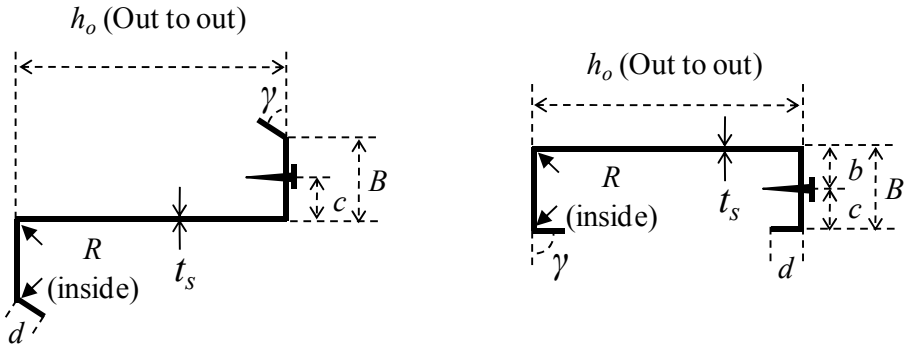

Fig. 2.10 Girt cross-section

Table 2.1 Specimen dimensions

Specimen name	h_o (mm)	t_s (mm)	B (mm)	b (mm)	c (mm)
Z200-1	203	2.59	66.2	---	28.7
Z200-2	203	2.59	65.8	---	34.0
Z250-1	254	2.69	65.6	---	33.0
Z250-2	254	2.69	67.2	---	35.8
C200-1	203	2.62	66.7	37.3	29.2
C200-2	203	2.62	65.3	29.2	30.0
C250-1	254	2.67	78.2	40.9	37.3
C150-1	152	1.76	50.1	24.1	26.7

2.3.2 Test setup

Each specimen was an assembly of 1- 1524mm long C- or Z-section cold-formed steel stud and 2- 0.46 mm thick 762 mm by 1524 mm panels (see Fig. 2.11). The two panels are joined using 6.4 mm diameter fasteners at the panel edges to form a 1524 mm by 1524 mm panel. The member flange is through-fastened to the panel with #12-14 self drilling screws every 305 mm (adjacent to the rib) as shown in Fig. 2.11. The base of each specimen was clamped between 152 mm by 102 mm by 7.9 mm steel angles as shown in Fig. 2.11. The angles have pre-drilled holes every 146 mm and are through-fastened and clamped with 15.8 mm diameter structural bolts. Plaster was poured 152 mm high in the voids between the angles and the metal panel ribs to prevent crushing of the panel.

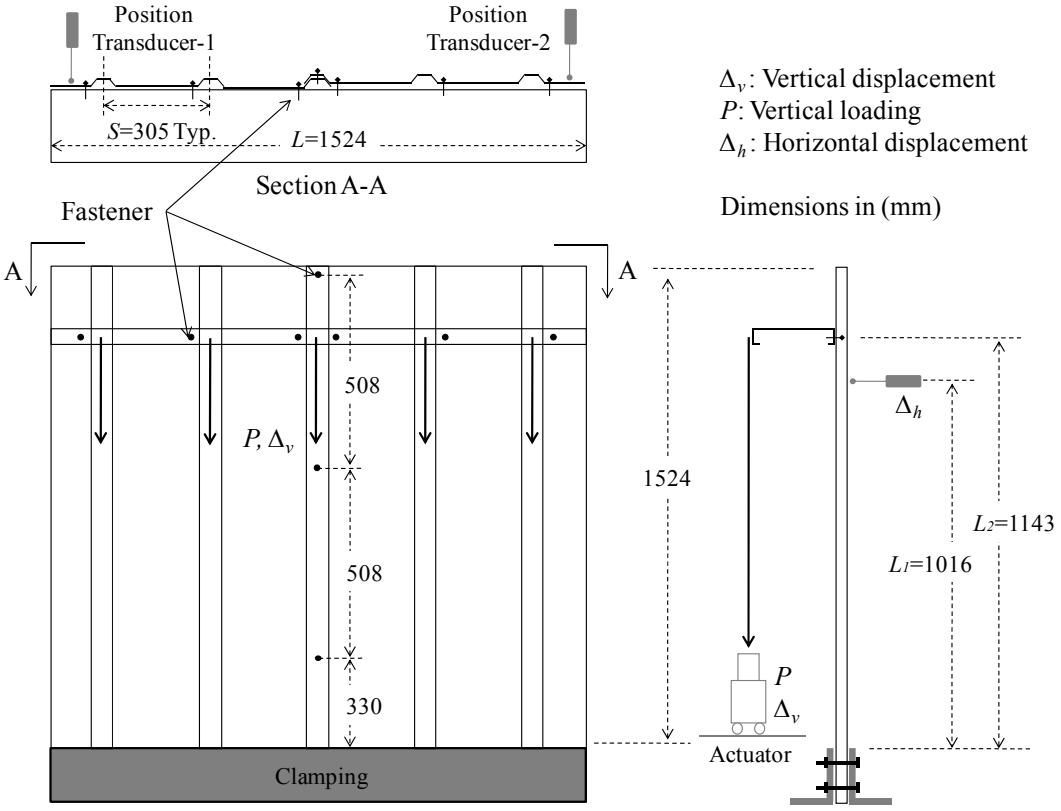

Fig. 2.11 Rotational restraint test setup

2.3.3 Test procedure and instrumentation

A uniformly distributed moment M was applied to the specimen with vertical force P/L applied at a moment arm of h_o on the cross-section free flange, where L is the girt length in Fig. 2.11. The actuator is free to move horizontally on rollers, keeping the load vertical as the specimen rotates. The total rotation (θ), which is the summation of wall panel bending (θ_w), connection rotation (θ_c) and web bending (θ_s) [12] is measured as shown in Fig. 2.12. The applied moment $M=Ph_o/L$, where h_o is the cross-section web depth, if small deformations are assumed.

A pair of position transducers is used to measure the horizontal deflection, Δ_h, of the panel. The transducers are set 127 mm below the horizontal row of fasteners to avoid the effect of panel local deformation. The vertical displacement, Δ_v, and the point loading, P, are recorded by an LVDT and load cell inside the actuator.

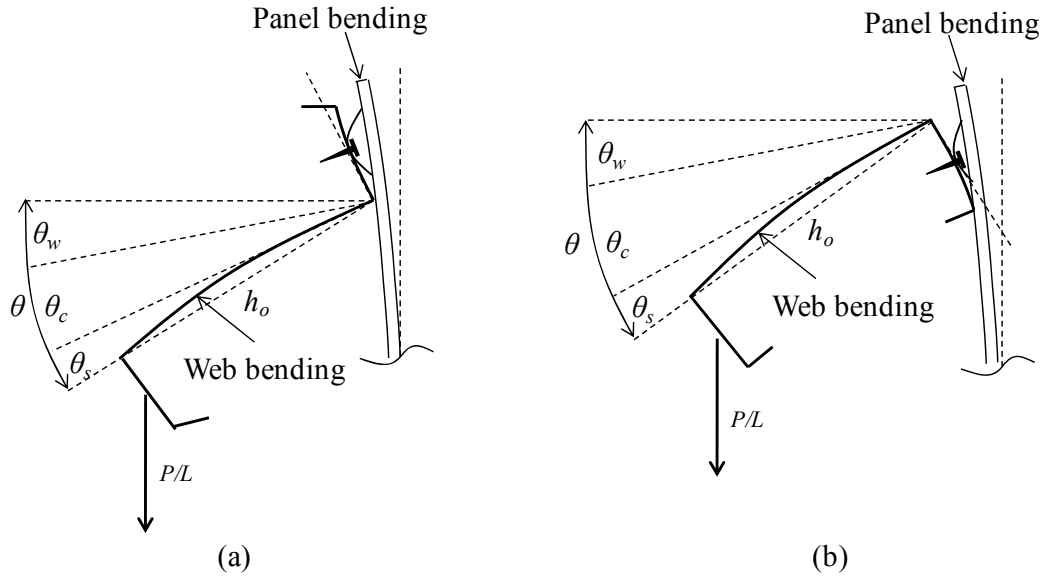

Fig. 2.12 Displaced shape during rotational restraint test for a (a) Z- section, (b) C-section

2.3.4 Isolating connection stiffness from the experimental data

The rotation from web bending, θ_s, is determined by assuming the web is a cantilever (Fig. 2.13b):

$$\theta_s = \frac{Ph_0{}^2 S}{3EIL} \ . \tag{2.8}$$

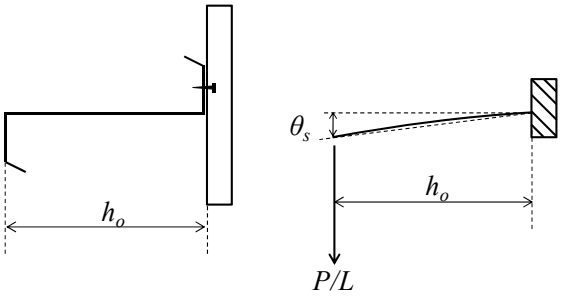

(a) (b)

Fig. 2.13 Rotation due to web bending

To calculate the rotation from panel bending, θ_w, the panel is treated as a cantilever beam with a distributed moment Ph_o/L applied at the free end through the member-panel connection (see Fig. 2.14), resulting in the following equations:

$$\theta_w = \frac{Ph_oL_1}{LEI_w} \tag{2.9}$$

$$\Delta_h = \frac{Ph_oL_2^2}{2LEI_w} \tag{2.10}$$

where EI_w is the wall panel flexural rigidity per unit length; Δ_h is the horizontal deflection measured by the position transducer during the test; L_1 is the distance between the fastener and the fixed end of the cantilever beam; L_2 is the distance between the position transducer and the fixed end of the cantilever beam (see Fig. 2.14). Solving Eq. (2.10) in terms of Δ_h and substituting into Eq. (2.9) leads to

$$\theta_w = \frac{2\Delta_h L_1}{L_2{}^2} \ . \tag{2.11}$$

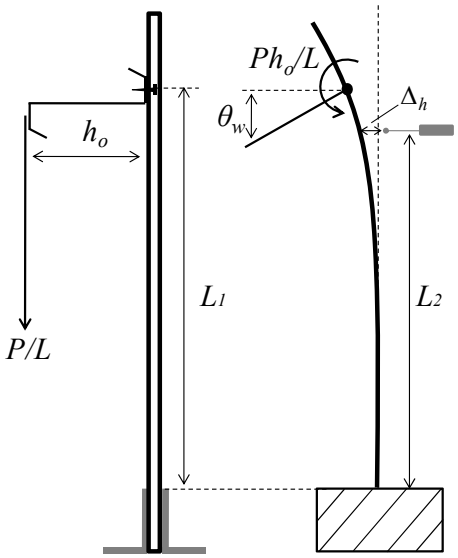

Fig. 2.14 Panel bending

The expressions in Eqs. (2.8) and (2.11) are used to isolate the experimental rotational connection stiffness and then compared to model predictions, i.e., Eq. (2.12), in the following section.

2.3.5 Test to predicted comparison

The predicted $\theta_c = M/k_{\phi c}$ for a C- or Z-section is calculated by assuming $M = Ph_o/L$

$$\theta_c = \frac{Ph_o}{Lk_{\phi c}} \quad . \tag{2.12}$$

The connection rotational stiffness $k_{\phi c}$ is calculated with Eq. (2.6) for a C-section and Eq. (2.7) for a Z-section. The panel stiffness at a screw k_p is obtained from Fig. 2.8 and the panel thickness t_w=0.46 mm. The measured connection rotation θ_c is obtained from the experimental results as

$$\theta_c = \theta - \theta_s - \theta_w \tag{2.13}$$

The predicted moment-rotation response is consistent with the experimental results as shown in Figs. 2.15 to 2.18. A linear region (shown between two ‘o’s in Figs.

2.15 to 2.18) was selected on each experimental moment-rotation curve to obtain the tested through-fastened connection rotational stiffness ($k_{\phi c}$). The experimental $k_{\phi c}$ is compared to the predicted $k_{\phi c}$ in Table 2.2. The test-to-predicted mean and COV are 1.01 and 0.05 respectively, demonstrating that Eq. (2.6) and Eq. (2.7) are viable predictors for the specimen and panel type considered. An example of how the rotational stiffness prediction can be used in a through-fastened girt or purlin elastic buckling analysis is provided in the next section.

Table 2.2 Comparison of the experimental and predicted $k_{\phi c}$ (slopes in Figs. 2.15 to 2.18)

Specimen name	Experimental $k_{\phi c}$ N-mm/rad/mm	Predicted $k_{\phi c}$ N-mm/rad/mm	Test/Predicted
Z200-1	994	1048	0.95
Z200-2	1339	1343	1.00
Z250-1	1342	1300	1.03
Z250-2	1423	1459	0.97
C200-1	941	895	1.05
C200-2	943	966	0.98
C250-1	1151	1199	0.96
C150-1	730	660	1.11

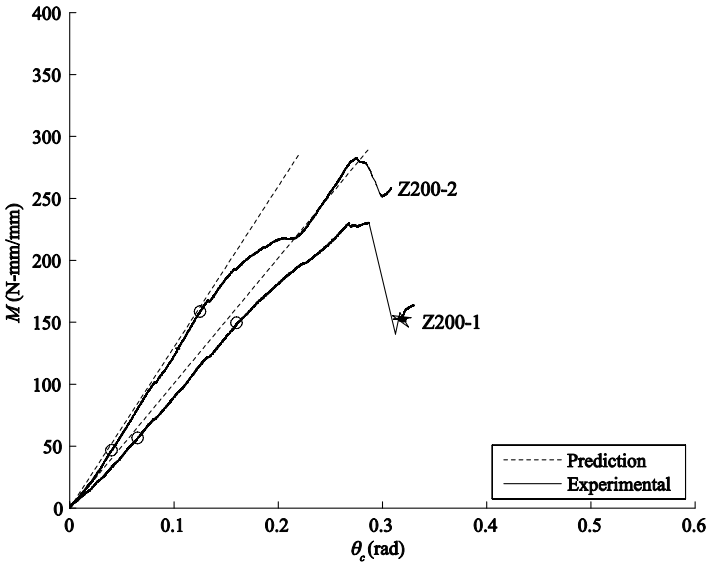

Fig. 2.15 Test to predicted comparison for Z-section specimens with h_o=200 mm.

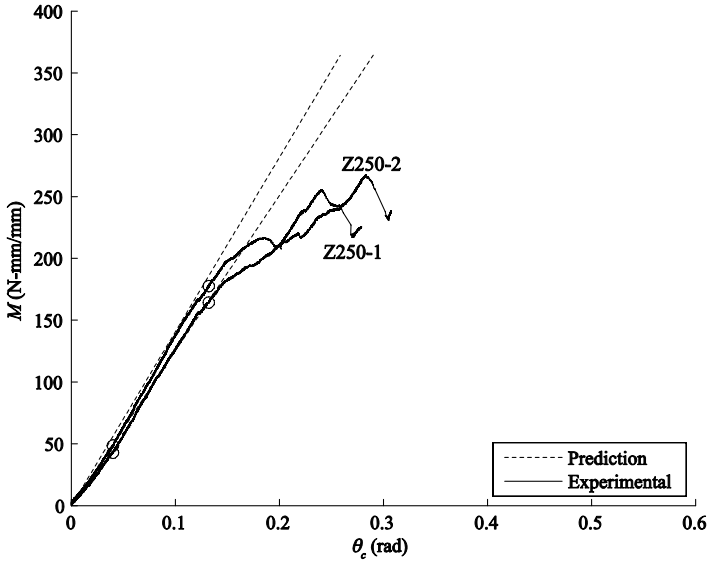

Fig. 2.16 Test-to-predicted comparison for Z-section with with h_o=250 mm

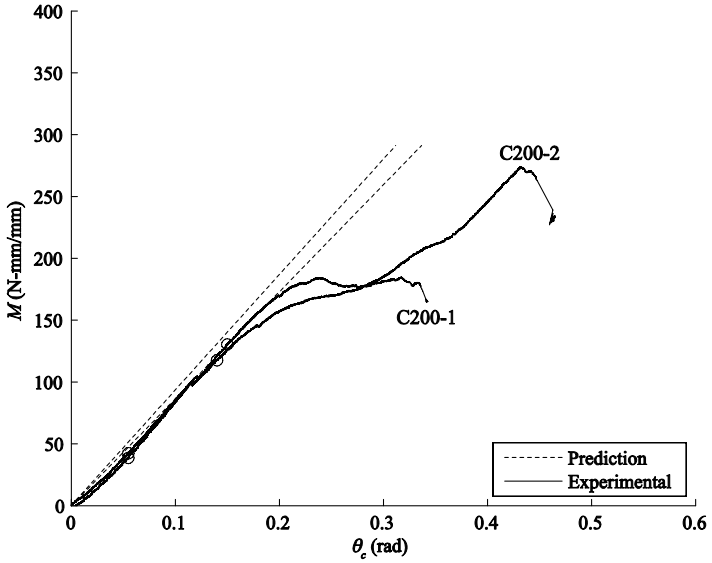

Fig. 2.17 Test-to-predicted comparisons for C-section with h_o=200 mm

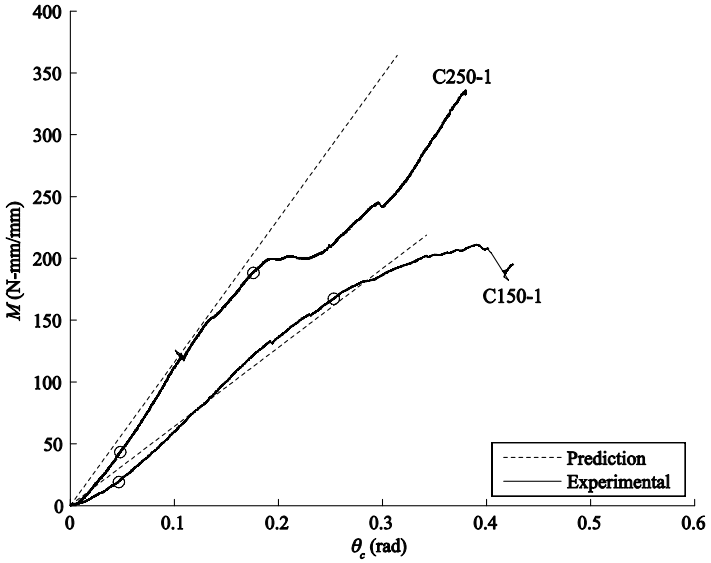

Fig. 2.18 Test-to-predicted comparisons for C-section with h_o=250 mm, 150 mm.

2.4 Example – including connection rotational restraint in an elastic buckling analysis

The mechanics-based expressions for rotational restraint in Eq. (2.6) for a C-section and Eq. (2.7) for a Z-section are used here with a finite strip eigen-buckling analysis in CUFSM with the goal of predicting the critical elastic global buckling moment (M_{cre}) including the influence of rotational restraint. The rotational stiffness is calculated using the metal panel and member dimensions of (h_o=200mm, B=75mm, t_s=2.5mm, d=25mm, c=37.5mm, b=37.5mm, R=5mm, γ=90^o, see Fig.10), resulting in $k_{\phi c}$=1285 N-mm/rad/mm for the Z-section and $k_{\phi c}$=1010 N-mm/rad/mm for the C-section. Even though the Z- and C-sections have the same cross-section dimensions, the through-fastened Z-section connection has a higher rotational stiffness because the fastened flange is more resistant to rotation than the C-section. This is one explanation for why Z-sections have had higher tested capacities than C-sections in past experimental research [34].

Rotational springs are input into a finite strip analysis as shown in Figs. 2.19 and 2.20. The location of the spring in the finite strip model on the cross-section is important because $k_{\phi c}$ includes the influence of flange bending. For a C-section, the spring is placed at the rotation pivot point defined by the flange-lip intersection, while for a Z-section the spring is placed at the web-flange intersection (again the rotation pivot point). For both cross-sections lateral translation is assumed to be fully braced by the screw connection, see the pinned support in Fig. 2.19 and Fig. 2.20.

Eigen-buckling analyses are performed at several half-wavelengths in CUFSM with and without the rotational spring, and the results are shown for both Z- and C-sections in Fig. 22 and 23. The reference stress applied to the cross section assumes restrained bending, i.e., the stress is calculated as My/I about the strong centroidal axis where the free flange is in compression. (This reference stress is used here just for example purposes, see [35] for details on how to calculate a more realistic reference stress for a purlin or girt loaded by wind uplift or wind suction.)

The rotational spring does not influence local buckling or distortional buckling because the spring is located on the tension flange away from buckling deformation. The spring does increase the global buckling moment, M_{cre}, compare 19.1×10^6 N-mm to 8.4×10^6 N-mm for the Z-section and 16.3×10^6 N-mm to 8.3×10^6 N-mm for the C-section. It is also observed that without a spring M_{cre} corresponds to the physical unbraced length of the member, L_b, however when a rotational spring is added, M_{cre} has a unique natural buckling half-wavelength, L_{cre}, which means that multiple half-waves could form within the physical length if $L_{cre}<L_b$.

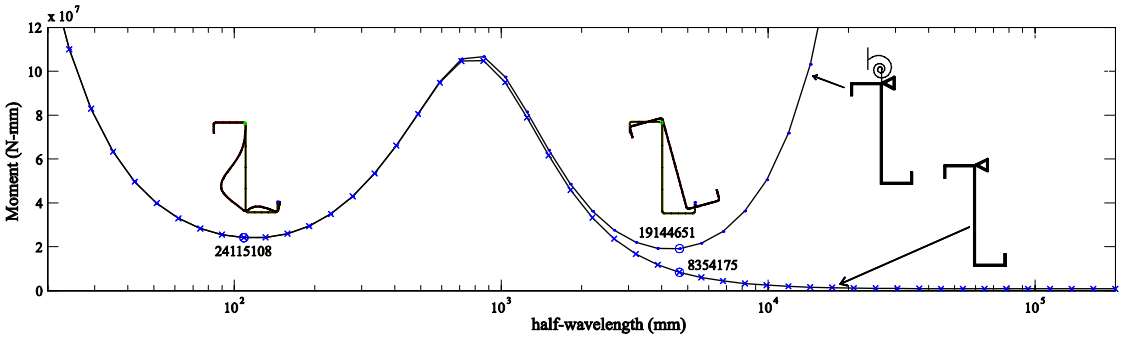

Fig. 2.19 Elastic buckling curve for Z- section including rotational restraint

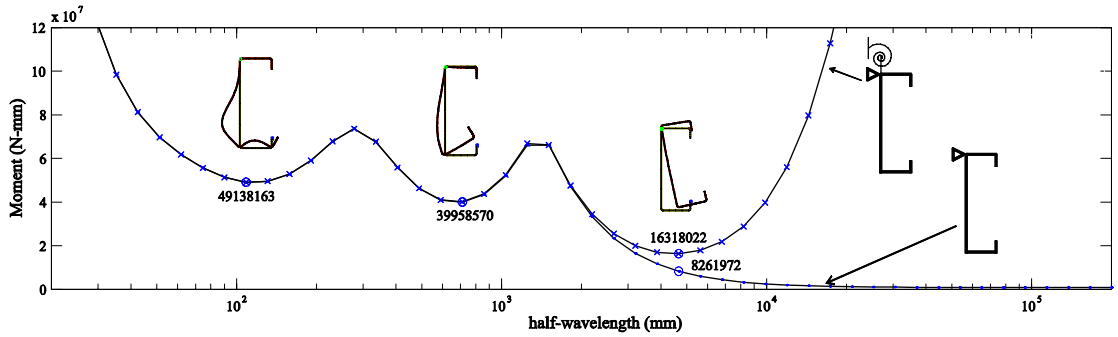

Fig. 2.20 Elastic buckling curve for a C-section including rotational restraint

2.5 Conclusions

Mechanics-based expressions were introduced for predicting through-fastened connection rotational restraint provided by a metal panel to a C- or Z-section girt or purlin. The equations account for the influence of panel deformation at the screw, and girt or purlin flange bending at the through-fastened connection. The panel stiffness at a screw was calculated for a typical panel cross-section with finite element parameter studies. Flange bending stiffness is typically higher for a Z-section than a C-section. A finite strip eigen-buckling analysis example demonstrated how a spring could be used to simulate rotational restraint from a through-fastened connection. The critical elastic lateral-torsional buckling moment increased when the spring was added, and a unique fundamental buckling half-wavelength was identified, suggesting that multiple half-waves can form within a girt or purlin unbraced length. This research is a key step

forward in developing an analytical strength prediction approach for through-fastened roof and wall systems.

Acknowledgements

The authors are grateful for the support of the Metal Building Manufacturers Association (MBMA) and the American Iron and Steel Institute (AISI). The experiments were conducted through a gracious collaborative effort by Dr. Ben Schafer in the Department of Civil Engineering at Johns Hopkins University.

References

[1] Yu WW, LaBoube RA. Cold-Formed Steel Design. 4th Edition. Hoboken, New Jersey: John Wiley & Sons, Inc., 2010.
[2] Zetlin L, Winter G. Unsymmetrical bending of beams with and without lateral bracing. ASCE Journal of Structural Division 1955; 81, 774-1.
[3] Thomasson PO, On the behaviour of cold-formed steel purlins-particularly with respect to cross sectional distortion. Baehre-Festschrift. Karlsruhe, Germany; 1988, 281-292.
[4] Murray T, Elhouar S. Stability requirements of Z-purlin supported conventional metal building roof systems. In: Annual Technical Session, Structural Stability Research Council. Cleveland, Ohio; 1985.
[5] Trahair NS. Flexural-torsional Buckling of Structures. Boca Raton, Florida: CRC Press, 1993.
[6] Peköz T, Soroushian P. Behavior of C- and Z-purlins under wind uplift. In: Sixth International Specialty Conference on Cold-Formed Steel Structures. Rolla, Missouri; 1982, 409-429.
[7] Rousch CJ, Rasmussen KJR, Hancock GJ. Bending strengths of cold-formed channel and Z-sections restrained by sheeting. In: International Workshop on Cold-formed Steel Structures. Sydney, Australia; 1993.
[8] Rousch CJ, Hancock GJ. Comparison of tests of bridged and unbridged purlins with a non-linear analysis model. Journal of Constructional Steel Research 1997; 41(2-3), 197-220.
[9] Vieria LCM, Malite M, Schafer BW. Simplified models for cross-section stress demands on C-section purlins in uplift. Thin-Walled Structures 2010;48(1), 33-41.
[10] Haussler RW, Pabers RF. Connection strength in thin metal roof structures. In: Second International Specialty Conference on Cold-Formed Steel Structures. St. Louis,

Missouri; 1973, 857-874.
[11] MRI. Determination of rotational restraint factor 'F' for panel to purlin connection rigidity. Observer's Report: MRI Project No. 7105-G. Midwest Research Institute, Kansas City, Missouri;1981.
[12] Schafer BW, Sangree RH, Guan Y. Experiments on rotational restraint of sheathing. Report for American Iron and Steel Institute-Committee on Framing Standards. Baltimore, Maryland; 2007.
[13] LaBoube RA. Roof panel to purlin connections: rotational restraint factor. In: IABSE Colloquium on Thin-Walled Metal Structures in Buildings. Stockholm, Sweden; 1986.
[14] Rousch CJ, Hancock GJ. Purlin-sheeting connection tests. Research report R724, School of Civil and Mining Engineering, The University of Sydney, Australia; 1996.
[15] Vieira LCM. Behavior and design of sheathed cold-formed steel stud walls under compression. Ph.D. thesis, Johns Hopkins University, Baltimore, MD, 2011.
[16] Hancock G, Celeban M. Healy C. Behaviour of purlins with screw fastened sheeting under wind uplift and downwards loading. Australian Civil Engineering Transactions 1993; CE35(3), 221-233.
[17] Rousch CJ. The behaviour and design of purlin-sheeting systems. Ph.D. thesis, The University of Sydney, Australia; 1996.
[18] Rousch CJ, Hancock GJ. Determination of purlin R-factors using a non-linear analysis. In: Thirteenth International Specialty Conference on Cold-formed Steel Structures. Rolla, Missouri; 1996.
[19] Lucas RM, Al-Bermani FGA, Kitipornchai S. Modelling of cold-formed purlin sheeting systems. Part 1: Full model. Thin-Walled Structures 1997; 27(3), 223-243.
[20] Lucas RM, Al-Bermani FGA, Kitipornchai S. Modelling of cold-formed purlin-sheeting systems. Part 2: Simplified model. Thin-Walled Structures 1997; 27(4), 263-286.
[21] Papangelis JP, Hancock GJ, Trahair NS. Computer design of cold-formed C- and Z-section purlins. Journal of Constructional Steel Research 1998; 46(1–3), 169–171.
[22] Clarke MJ, Hancock GJ. Purlin design to AISI LRFD using rational buckling analysis. In: Fifteenth International Specialty Conference on Cold-formed Steel Structures. Rolla, Missouri; 2000.
[23] Quispe L, Hancock GJ. Direct strength method for the design of purlins. In: Sixteenth International Specialty Conference on Cold-formed Steel Structures. Orlando, Florida; 2002, 561-72.
[24] Pham CH, Hancock GJ. Direct strength design of cold-formed purlins. Journal of Structural Engineering 2009; 135(3), 228-238.
[25] Gao T, Moen CD. Flexural capacity prediction of metal wall girts: using the direct strength method. In: Sixth European Conference on Steel and Composite Structures. Budapest, Hungary; 2011.
[26] EN-1993. Eurocode 3: Design of Steel Structures. European Committee for Standardization, Brussels, Belgium; 2006.
[27] Schafer BW, Adany S. Buckling analysis of cold-formed steel members using CUFSM: conventional and constrained finite strip methods. In: Eighteenth International Specialty Conference on Cold-Formed Steel Structures, Orlando, Florida; 2006.
[28] AISI-S100. North American Specification for the Design of Cold-Formed Steel

Structural Members. Washington, D.C.: American Iron and Steel Institute, 2007.
[29] Gao T, Moen CD. Flexural capacity prediction of metal building wall girts with the Direct Strength Method. In: Eurosteel. Budapest, Hungary; 2011.
[30] Gao T, Moen CD. Flexural strength of exterior metal building wall assemblies with rigid insulation. In: Structural Stability Research Council Annual Conference. Grapevine, Texas; 2012
[31] ABAQUS. ABAQUS/Standard Version 6.7-3. Providence, RI: Dassault Systèmes, http://www.simulia.com/, 2007.
[32] Timoshenko SP. Theory of Plates and Shells. New York: McGraw-Hill, 1940.
[33] Nowinski J. Note on an analysis of large deflections of rectangular plates. Applied Scientific Research 1963; 11(1), 85-96.
[34] Fisher JM. Uplift capacity of simple span Cee and Zee members with through-fastened roof panels. Final report: MBMA 95-01. Metal Building Manufacturers Association, Cleveland, Ohio; 1996.
[35] Gao T, Moen CD. Direct Strength Flexural Capacity Prediction of Through-Fastened Cold-Formed Steel Roof Purlins and Wall Girt Systems Wind Uplift or Suction. In: Twenty-First International Specialty Conference on Cold-formed Steel Structures. St. Louis, Missouri; 2012.

Chapter 3: Flexural Strength Experiments on Exterior Metal Building Wall Assemblies with Rigid Insulation

*(*Submitted to *Journal of Constructional Steel Research)*

"Flexural Strength Experiments on Exterior Metal Building Wall Assemblies with Rigid Insulation"

Abstract

This research program evaluated the flexural capacity of a metal building wall system with rigid board foam insulation sandwiched between C- and Z-section girts and through-fastened steel panels. Vacuum box tests were conducted to simulate wind suction on the wall system, and distinct failure modes were observed. The metal panel pulled over the screw heads for wall systems without insulation, however when rigid board insulation was added, the insulation acted as a washer and girt failure or screw fracture was observed. Screw bending and fracture were common in the specimens with the thickest rigid board insulation and for locally stocky cross-sections because a concentrated moment could be developed in the fastener. In these cases wall system capacity was decreased by the presence of rigid board insulation. For wall system specimens with locally slender girts, rigid board insulation did not influence girt capacity because girt deformation under load was primarily in the cross-section and not at the through-fastened connections.

3.1 Introduction

The critical load case for cold-formed steel wall girts in a metal building wall system is suction caused by wind. As wind pulls the wall away from the building, the girt unbraced flanges are placed in compression, resulting in lateral-torsional buckling deformation that is partially restrained by the through-fastened panel connection. Girt deformation (rotation) is amplified by strong-axis bending induced shear flow (Fig. 3.1) that causes the web and free flange to deform relative to the connection [1-3].

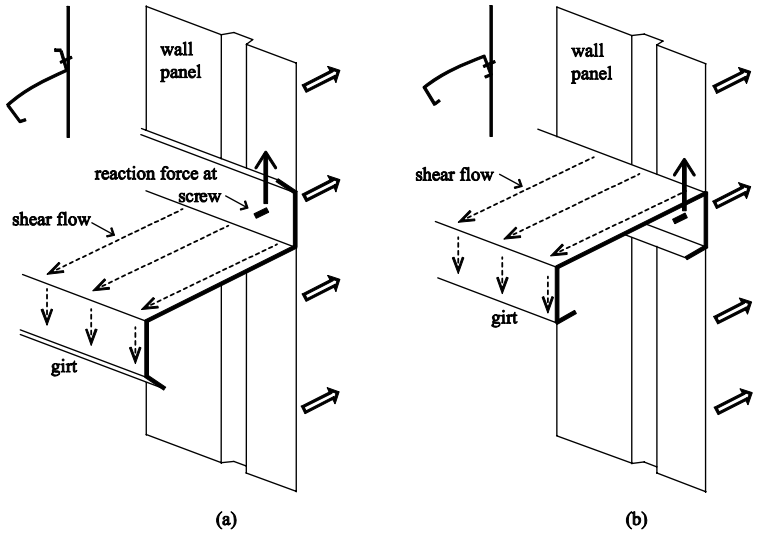

Fig. 3.1 Girt rotation due to the shear flow in (a) a C-section, and (b) a Z-section

Girt flexural capacity is strongly influenced by the amount of rotational restraint provided by through-fastened connections to the metal wall panel [4-7]. In North America and Australia, rotational restraint on girt flexural capacity, M_n, is considered for the wind suction case in experimentally derived strength reduction factors, i.e., R-factors, as described in AISI S100-07 D6.1.1 [8] and AS/NZS 4600 3.3.3.4 [9], where $M_n=RF_yS_e$ and S_e is the effective section modulus of the girt about its strong centroidal axis including local buckling. In Europe [10], the free compressed flange is treated as a column on an elastic foundation [11], where the foundation spring, representing the restraint provided by the web and through-fastened connection, is calculated with empirical equations derived from experiments [4,5].

The worldwide sustainability movement is motivating design and construction code changes that emphasize energy efficiency (e.g., ASHRAE-90.1 2010) [12]. To meet these stringent energy standards, the metal building industry is exploring alternative insulation materials to fiberglass blanket. One option for providing a continuous thermal barrier is rigid board insulation, typically a polyisocyanurate foam with trilinear stress-

strain properties in compression [13, 14]. The insulation board is manufactured in different thicknesses, most commonly 25.4 mm and 50.8 mm, and it has been installed in thicknesses as high as 101.6 mm [15].

Rotational restraint studies with rigid board insulation through-fastened between a girt and metal panel have shown that rotational restraint increases as a function of rigid board insulation thickness [7]. The insulation acts as a washer against the metal panel, spreading the fastener force and reducing local deformation in the metal panel (Fig. 3.2). Rotational stiffness is also influenced by the compressive stress-strain properties of the rigid board insulation because as the girt tends to rotate under load, the pivot point on the flange indents the insulation. Rotational restraint mimics the insulation trilinear compressive stress-strain curve – initially very stiff until the cell walls of the foam buckled, then a region of lower stiffness as the air voids in the insulation are compressed, and a third region of increased stiffness because of the higher material density [7].

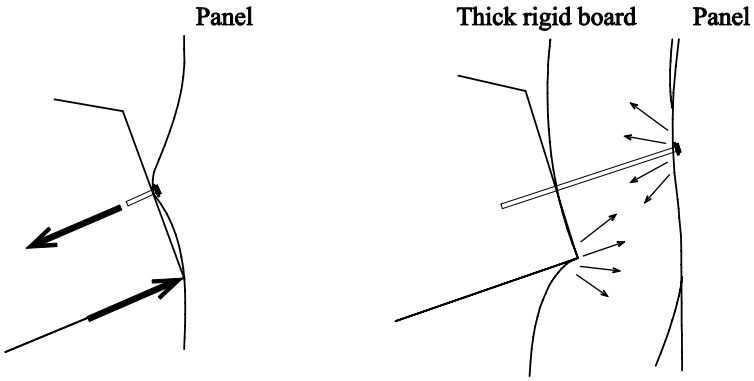

Fig. 3.2 Rigid board influences girt rotational restraint: fastener force spreads out across panel [16]

The goal of the research study summarized herein was to experimentally observe and quantify the influence of rigid board insulation on through-fastened wall girt flexural capacity. The test program studied wall systems with varying rigid board insulation thicknesses (25.4 mm, 50.8 mm, 2 x 50.8 mm) using vacuum box tests. The experimental

details, strength comparisons and failure modes are discussed and documented in the following sections.

3.2 Experimental program

3.2.1 Test setup

The test setup was designed to simulate exterior wind suction that pulls a wall outward and away from a metal building, placing the free girt flanges in compression. Each wall specimen was constructed with two simple span parallel girts with their free flanges facing up in the box. The girts span 7468 mm between bearing centerlines (Fig. 3.3) and they are through-fastened to a wall panel (4140 mm wide) at a spacing of 2286 mm. The pressure box is sealed with plastic sheeting from above and air is pulled out below the specimen with vacuum pumps to simulate the suction loading.

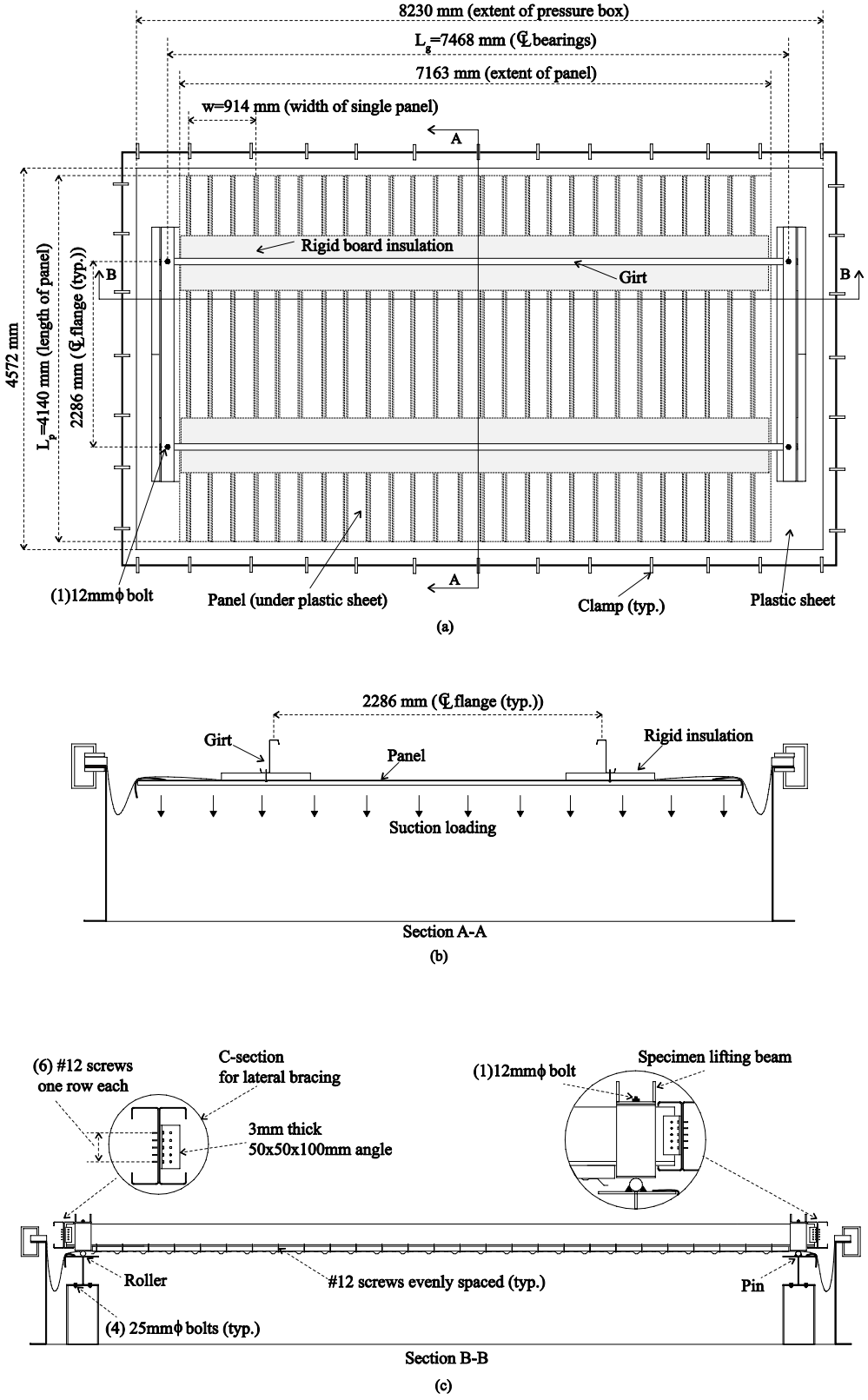

Fig. 3.3 (a) Test setup plan (b) elevation section A-A (c) elevation section B-B

3.2.2 Test matrix

A total of 50 pressure box experiments were performed with the test matrix in Table 1. The specimen naming convention is: girt profile (C- or Z-section), nominal web depth, metal panel type (Durarib or Bigbee), insulation type (R: fiberglass blanket; TH: Thermax), insulation thickness, specimen number within a specific series (1 or 2) and fastener with a washer (W). The girt cross-section dimensions were selected to explore the dimensional limits specified in the North American R-factor strength prediction approach (AISI 2007, Section D6.1.1) [8] summarized in Table 3.1, i.e., partially effective (locally slender) and fully effective (locally stocky) C- and Z-sections were chosen.

Dow Thermax rigid board insulation was the focus of this study (Tests 16-50 in Table 3.1), although bare panel tests (Tests 1-13 in Table 3.1) and tests with fiberglass blanket insulation (R-value of 13 [17]) (Tests 14-15 in Table 3.1) were also performed to provide a baseline for evaluating the influence of rigid board on wall girt capacity. The bare panel and R13 tests also accommodated a comparison between this test setup and existing data that was used to define the current AISI R-factors [18]. The R13 fiberglass insulation uncompressed thickness was 101.6 mm. The influence of rigid board insulation thickness was evaluated with tests employing 1- 25.4 mm insulation sheet, 1- 50.8 mm sheet, and 2 - 50.8 mm (101.6 mm total) sheets.

Metal panel profile, thickness, and stress-strain properties have all been shown to influence rotational restraint [4, 6]. In this study, two 26 gauge (0.46mm thick) panels types (NCI Durarib and Bigbee), were used with dimensions shown in Fig. 3.4. The 26 gauge panel was selected because this is the minimum allowable thickness specified in

the North American specification for the R-factor method (AISI 2007, Section D6.1.1). The yield stress for each panel type was measured with uniaxial tensile coupon tests [19], with the Durarib panel having 380 MPa yield stress and a ductile failure at 22% engineering strain and the Bigbee panel having 620 MPa yield stress and a more brittle failure at approximately 10% engineering strain.

Two sizes of screws without washers were used to fasten the panel to the girts: 127 mm long #1/4-14 self-drilling screws were used for the test specimens with the thickest rigid board insulation (101.6 mm, see "TH100" in Table 1) and #12 screws for all other test specimens. The #1/4-14 and #12 screw diameters including the threads were measured to be 5.36 mm and 4.62 mm, respectively. In Test 5 only (Z girts, Bigbee, no insulation) #12 screws with 14.5 mm diameter washers were used.

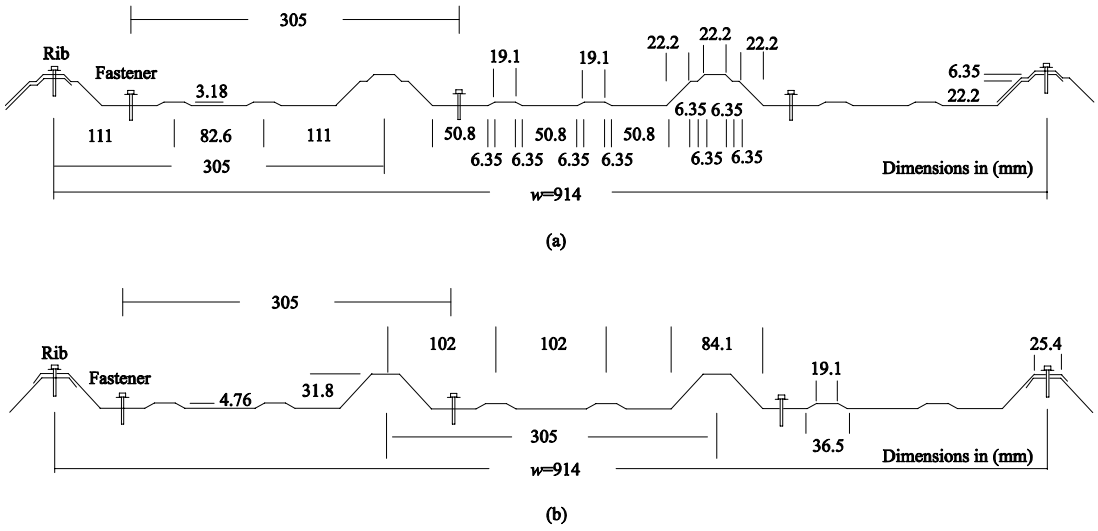

Fig. 3.4 Cross-section of (a) Durarib and (b) Bigbee and fastener location

3.2.3 Test boundary conditions

The support boundary conditions were a roller and pin as shown in Fig. 3.3. A transverse screw-fastened C-section brace was installed before each test to provide girt lateral restraint at the supports (Fig. 3.3). The advantages of this test setup are that the

influence of catenary action (i.e., tension stiffening) is eliminated and the girt moment distribution (parabolic) and moment magnitude ($wL^2/8$) are known, making comparisons of tested strength to strength predictions straightforward. The disadvantage of this test setup is that it is not representative of the actual boundary conditions in a metal building where the bottom flange is bolted to the primary frame.

3.2.4 Specimen construction

Each wall specimen was constructed with a special jig that held the two girts in place while the metal panels were through-fastened to the girts at a 305 mm spacing. The specimens were constructed with the panel facing up to accommodate fastener placement, and then the wall was flipped over with an overhead crane and placed in the pressure box, see [16] for details. The screws fastening the panel to the girts were installed adjacent to the rib (consistent with industry practice), and the screws lapping the panel were installed at the middle of the rib (see Fig. 3.4).

Preliminary tests demonstrated that the 26 gauge metal panels failed before the girts because the tested boundary conditions for the panels are not continuous in flexure, causing large moments at the transverse panel midspan. To prevent panel flexural failure, the panels were stiffened with 1524 mm wide 26 gauge panel strips at midspan. The reinforcement was made narrow enough to avoid interference with the girt-panel connection zone.

Rigid board insulation strips 610 mm wide were fixed to the girt flanges with self-drilling screws, and then the metal panels were through-fastened to the girt flanges. The insulation was sandwiched between the panels and flanges. Although the flange centerlines were approximately marked on the panels, it was still difficult to install the

screws at the center of the flange because of the rigid board thickness. The screw locations on the flange were measured after each test as described in the following section.

3.2.5 Specimen measurements and material properties

Measured girt cross-section out-to-out dimensions (Fig. 3.5) and base metal thickness for the tested girts are provided in Table 1. The inside radii were measured at four flange/lip or flange/web corners and the average is provided in Table 3.1. The base metal thickness is measured from tensile coupon test specimens and the average is provided in Table 3.1. Girt sweep was measured at midspan on the free flange by running a string line as illustrated in Fig. 3.7. The yield stress was measured with tensile coupons cut from the girt flanges and web [16], the average of which is provided in Table 3.1.

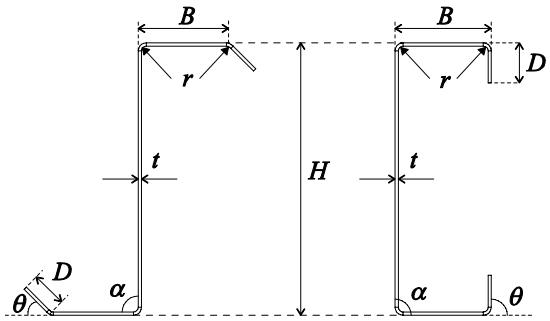

Fig. 3.5 Cross-section dimension notation

Table 3.1 Specimen dimensions, sweep imperfections and yield stress

#	Test name	Cross-section											Girt sweep at midspan	F_y
		Compression flange				Tension flange								
		B	D	α	θ	B	D	α	θ	H	r	t		
		mm	mm	deg.	deg.	mm	mm	deg.	deg.	mm	mm	mm	mm	MPa
1	Z200D-1	-	-	-	-	-	-	-	-	-	-	-	-	-
2	Z200D-2	68.4	26.4	92	47	72.5	27.5	92	53	202	6.6	2.59	-	420
3	Z200D-3	68.1	25.2	91	47	65.5	25.7	90	53	204	8.2	2.54	-	415
4	Z200B-1	68.6	24.4	90	47	70.1	28.0	90	52	205	7.3	2.57	-	433
5	Z200B-2W	68.0	25.8	91	46	70.1	26.1	91	53	204	6.7	2.57	0.3	418
6	Z250D-1	72.0	19.8	90	55	73.3	20.3	91	46	253	7.0	1.52	0.1	403
7	Z250D-2	72.0	20.8	90	55	72.6	21.4	90	48	253	6.5	1.52	1.8	401
8	Z250B-1	71.7	21.1	91	55	72.9	22.1	90	47	253	5.9	1.51	-0.3	401
9	Z250B-2	70.7	22.3	91	54	73.3	20.3	91	47	251	6.1	1.50	-3.1	399
10	C200D-1	65.2	21.3	92	90	65.0	21.7	92	90	203	5.1	2.57	-13.0	522
11	C200D-2	65.8	21.3	88	90	64.5	21.3	88	90	203	5.8	2.57	-8.3	519
12	C250D-1	64.5	20.9	90	89	65.5	19.6	90	89	254	5.6	1.49	0.3	423
13	C250D-2	63.8	20.8	89	91	65.0	19.3	89	91	254	5.5	1.50	-3.0	414
14	Z200D-R100-1	67.9	25.2	90	48	67.9	27.6	90	53	205	5.7	2.54	-	428
15	Z200D-R100-2	67.9	25.6	90	47	67.9	26.5	90	52	205	6.3	2.51	-	418
16	Z200D-TH25-1	70.6	25.3	92	46	70.8	28.0	91	52	204	7.1	2.54	-	428
17	Z200D-TH25-2	66.1	26.3	90	47	69.4	26.3	89	53	205	6.3	2.54	-	418
18	Z200D-TH50-1	73.3	24.1	91	48	69.3	26.2	90	53	202	7.7	2.57	-	423
19	Z200D-TH50-2	68.8	26.1	91	47	66.8	21.3	91	52	201	10.5	2.57	-	426
20	Z200D-TH100-1	69.7	22.6	92	47	70.1	26.7	90	53	201	7.6	2.57	-	427
21	Z200D-TH100-2	69.6	25.2	90	46	70.8	28.5	90	54	203	6.9	2.59	-	421
22	Z200B-TH25-1	70.0	26.2	90	46	70.3	27.8	88	53	204	6.1	2.54	-	421
23	Z200B-TH25-2	68.9	26.6	91	46	68.1	26.7	91	53	204	6.5	2.54	-	420
24	Z200B-TH50-1	72.1	25.1	89	48	71.4	28.0	89	53	203	7.5	2.57	-	424
25	Z200B-TH50-2	68.0	25.2	90	47	68.7	26.8	90	53	206	7.7	2.57	-	424
26	Z200B-TH100-1	68.1	26.0	90	47	68.7	25.0	90	52	202	6.7	2.57	-5.4	421
27	Z250D-TH25-1	68.4	20.1	92	54	73.9	20.8	91	47	253	6.5	1.50	-	404
28	Z250D-TH25-2	67.7	18.7	91	55	72.6	20.2	90	47	254	5.6	1.50	-	409
29	Z250D-TH50-1	67.2	21.1	90	54	71.9	20.7	91	47	252	6.5	1.54	-3.9	405
30	Z250D-TH50-2	71.9	20.1	91	56	72.9	20.6	91	47	253	6.3	1.54	2.9	402
31	Z250D-TH100-1	71.9	21.9	91	55	71.6	19.9	90	48	257	6.9	1.52	2.1	397
32	Z250D-TH100-2	72.0	22.0	90	54	73.0	20.0	90	46	253	6.1	1.52	8.3	409
33	Z250B-TH25-1	74.7	22.0	91	55	70.2	21.5	91	47	254	6.0	1.50	5.4	402
34	Z250B-TH25-2	69.3	20.4	90	55	72.5	20.1	89	47	258	6.2	1.52	1.5	398
35	Z250B-TH50-1	69.4	19.1	90	55	71.2	20.5	90	48	253	5.9	1.52	0.1	398
36	Z250B-TH50-2	68.0	19.4	90	55	70.0	19.8	90	48	254	5.7	1.52	3.9	402
37	Z250B-TH100-1	68.0	18.0	90	53	72.9	20.0	88	45	254	5.1	1.52	6.4	388
38	Z250B-TH100-2	68.1	22.6	90	54	72.8	20.2	88	47	254	6.8	1.52	2.9	409
39	C200D-TH25-1	63.8	21.0	93	90	64.5	21.0	93	90	203	4.8	2.57	-10.1	525
40	C200D-TH25-2	66.8	20.3	92	90	64.4	20.9	92	90	203	4.6	2.57	-12.8	526
41	C200D-TH50-1	61.5	21.2	91	90	62.8	20.2	91	90	203	4.0	2.58	-12.5	514
42	C200D-TH50-2	62.3	20.1	88	90	68.0	21.7	88	90	203	5.8	2.57	-8.3	531
43	C200D-TH100-1	64.7	21.2	87	90	65.7	21.0	87	90	203	6.3	2.57	-10.4	541
44	C200D-TH100-2	64.4	21.3	88	91	64.9	21.1	88	91	203	4.6	2.57	-7.9	547
45	C250D-TH25-1	63.1	21.2	89	90	63.2	20.9	89	90	254	4.3	1.49	-5.2	411
46	C250D-TH25-2	62.9	20.9	89	89	64.4	20.3	89	89	254	4.3	1.50	-3.4	410
47	C250D-TH50-1	63.1	20.1	90	90	68.1	21.3	90	90	254	4.8	1.50	-0.3	413
48	C250D-TH50-2	63.1	21.1	90	90	68.8	19.0	90	90	254	5.6	1.50	0.3	413
49	C250D-TH100-1	64.1	19.7	90	89	65.2	18.9	90	89	254	4.4	1.50	1.9	417
50	C250D-TH100-2	62.7	20.7	90	91	65.0	18.0	90	91	254	4.8	1.50	2.6	413

Name convention: girt profile, web depth, panel type (D=Duarib, B=Bigbee), - ,insulation type, insulation thickness, - ,series number, washer
#1/4-14 self-drulling screws for "TH100" tests; #12 self-drilling screws for all other tests

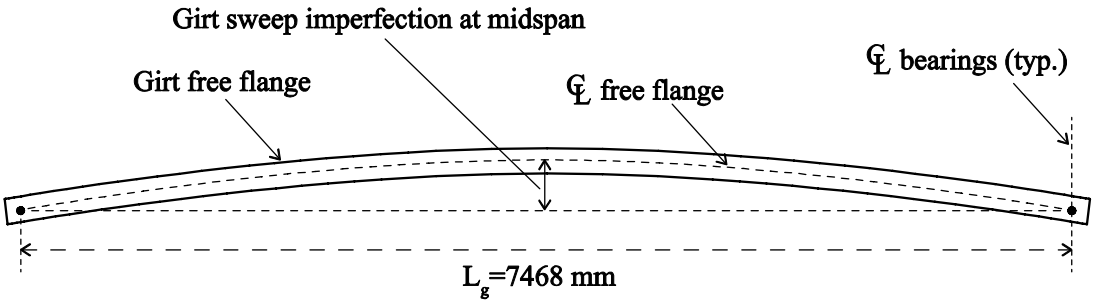

Fig. 3.6 Girt sweep imperfection at midspan

3.2.6 Instrumentation

A Vishay Micro-Measurements Model 5100B data acquisition system was used to digitally record six data channels at 10 points per second. Two pressure transducers with an accuracy of ±15 Pa were used to measure the pressure inside the vacuum box. The transducers were calibrated with a water tube manometer with a procedure documented in [20]. Four wire potentiometers with an accuracy of ±0.4 mm were mounted to a steel angle resting on the girt free flanges. They measured the vertical and lateral displacement at the intersection of the free flange and web at midspan, see [16] for instrumentation details. Video cameras recorded girt deformation during each test, see [21] to view the videos.

3.2.7 Test procedure

Before recording data, the vacuum pump was turned on with all vents open for one minute to zero the pressure. Immediately after data and video collection began, two supplemental vacuums were turned on, followed by the manual closing of the vents until specimen failure. The loading rate could not be finely controlled; however, the loading rate was approximately 10 Pa/sec.

3.3 Test results

3.3.1 Flexural capacity

The R-factor is calculated as:

$$R = \frac{M_{test}}{S_e F_y} \times 10^6 \tag{3.1}$$

where S_e is the effective section modulus obtained with the commercial software CFS [22] based on the measured girt dimensions shown in Table 3.1; F_y is the yield stress shown in Table 3.1; and M_{test} is the failure moment calculated as

$$F\,(\text{N/m}) = \frac{p_{test}(L_p/2)}{1000} + \frac{1000(d_p/2)}{w} + \frac{1000 d_g}{L_g} \tag{3.2}$$

$$M_{test}\,(\text{kN - m}) = \frac{F \times (L_g/1000)^2}{8} / 1000 \tag{3.3}$$

where the panel length L_p=4140 mm; the girt span L_g=7468 mm; the weight of a single (w by L_p, see Fig. 3.3 and 3.4) metal panel d_p=156N; the girt weight d_g=525N (Z200), 356N (Z250), 507N (C200), 347N(C250). The maximum pressure p_{test}, effective modulus S_e, peak girt moment M_{test}, R-factor are summarized in Table 3.2.

It has been shown by Gao and Moen [6, 7] that the rotational restraint provided to the girt is dependent on the screw location, c, which is the distance between the girt bearing pivot point and the center of the screw hole (see Fig. 3.7). Since the girt capacity was expected to be sensitive to c, it was measured for each specimen after a test (see Table 3.2), and overall variability in c is summarized in Table 3.3. Specifically, the distance between the pivot point and the screw hole edge, e, was measured with a digital caliper on failed girts over the middle half of the span. Screw location, c, is the average e plus half of the screw's diameter, $\phi/2$, as shown in Fig. 3.7. On average the fastener was

located close to the center of the flange (*c/B* is near 0.50 in Table 3.3), however variability was high. The screw location coefficient of variation (COV) in Table 3.3 was 20% for the case of the bare panel and thinner rigid board insulation, and increased to about 30% for thicker insulation because finding the center of the flange was difficult with a long screw driven through insulation. The relationship between *c* (as well as other test variables) and the failure mode trends in Table 3.2 are discussed in the following section.

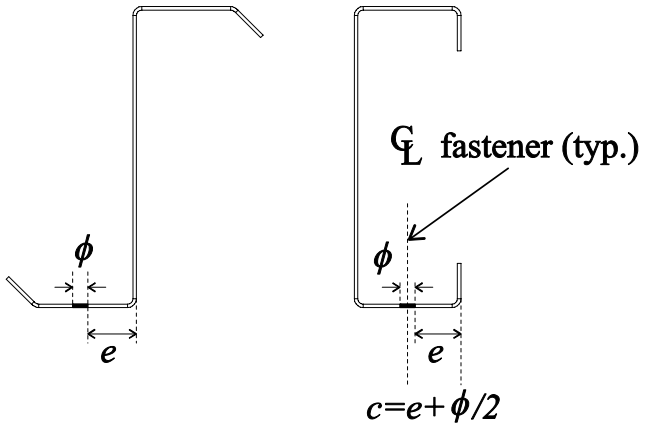

Fig. 3.7 Screw location *c* measurement

Table 3.2 Flexural capacity and R-factors

#	Test name	p_{test} (Pa)	S_e (mm^3)	M_{test} (kN-mm)	R	c (mm)	R_a	c_a	m	R^*	Failure mode
1	Z200D-1	-	-	-	-	-	-	-	-	-	1
2	Z200D-2	790	58600	11900	0.48	39	0.48	38	0.0079	0.46	2
3	Z200D-3	760	57400	11500	0.48	37					2
4	Z200B-1	870	56900	13100	0.53	41	0.53	41		0.48	2
5	Z200B-2W	890	58300	13500	0.55	36	0.55	36		0.54	2
6	Z250D-1	460	35800	7100	0.49	35	0.49	33	0.0020	0.49	4
7	Z250D-2	450	36300	7000	0.48	31					4
8	Z250B-1	440	36100	6800	0.47	25	0.48	34		0.49	4
9	Z250B-2	480	36700	7300	0.50	42					4
10	C200D-1	800	51000	12100	0.45	34	0.43	30	0.0079	0.45	2
11	C200D-2	690	51000	10600	0.40	26					2
12	C250D-1	330	33700	5200	0.36	20	0.37	20	0.0091	0.48	4
13	C250D-2	330	34000	5200	0.37	21					4
14	Z200D-R100-1	810	57600	12200	0.50	40	0.40	31	0.0079	0.43	2
15	Z200D-R100-2	470	58100	7400	0.31	21					2
16	Z200D-TH25-1	770	57300	11700	0.48	37	0.49	41		0.44	2,3,4
17	Z200D-TH25-2	820	58800	12400	0.50	45					2,3,4
18	Z200D-TH50-1	850	55600	12800	0.55	37	0.53	37		0.52	3,4
19	Z200D-TH50-2	800	55100	12200	0.52	36					3,4
20	Z200D-TH100-1	720	54400	11000	0.48	28	0.54	41		0.49	4
21	Z200D-TH100-2	960	57300	14500	0.60	53					4
22	Z200B-TH25-1	870	58300	13100	0.53	42	0.47	37		0.47	2,3,4
23	Z200B-TH25-2	650	58800	10000	0.41	32					2,3,4
24	Z200B-TH50-1	1010	57100	15100	0.63	47	0.59	44		0.52	3,4
25	Z200B-TH50-2	910	58100	13800	0.56	40					3,4
26	Z200B-TH100-1	850	57500	12900	0.53	34	0.53	34		0.53	4
27	Z250D-TH25-1	470	35400	7200	0.50	39	0.50	37	0.0020	0.50	4
28	Z250D-TH25-2	460	34700	7100	0.50	36					4
29	Z250D-TH50-1	430	35700	6600	0.46	28	0.48	29	0.0098	0.54	4
30	Z250D-TH50-2	460	35700	7100	0.50	30					4
31	Z250D-TH100-1	560	37700	8500	0.57	44	0.50	38		0.48	4
32	Z250D-TH100-2	430	36600	6600	0.44	31					4
33	Z250B-TH25-1	410	37300	6400	0.42	27	0.49	33		0.51	4
34	Z250B-TH25-2	530	36500	8000	0.55	39					4
35	Z250B-TH50-1	560	34800	8500	0.61	41	0.59	40		0.54	4
36	Z250B-TH50-2	530	34900	8000	0.57	39					4
37	Z250B-TH100-1	510	34200	7800	0.59	37	0.57	39		0.53	4
38	Z250B-TH100-2	540	37200	8200	0.54	40					4
39	C200D-TH25-1	460	50900	7300	0.27	20	0.29	23	0.0079	0.36	2,3
40	C200D-TH25-2	510	49800	8000	0.30	26					2,3
41	C200D-TH50-1	560	50900	8700	0.33	21	0.35	23		0.43	3
42	C200D-TH50-2	650	50400	10000	0.38	24					3
43	C200D-TH100-1	820	50500	12400	0.46	26	0.38	19		0.49	4
44	C200D-TH100-2	540	50300	8300	0.30	12					3
45	C250D-TH25-1	290	34300	4600	0.32	22	0.37	27	0.0091	0.42	4
46	C250D-TH25-2	380	34100	5900	0.42	33					4
47	C250D-TH50-1	300	33300	4800	0.35	22	0.30	17		0.44	4
48	C250D-TH50-2	220	34100	3500	0.25	12					4
49	C250D-TH100-1	320	33200	5100	0.37	22	0.41	26		0.48	4
50	C250D-TH100-2	420	34000	6500	0.46	30					4

Failure modes:

1: Panel flexual failure
2: Panel pull-over
3: Screw fracture and/or plastic bending
4: Girt failure

Table 3.3 Variation of screw location *c*

Insulation	Sample size (n)	*c/B*	
		Mean	COV (%)
Panel&R100	14	0.46	24%
TH25	12	0.48	21%
TH50	12	0.45	31%
TH100	11	0.47	32%

3.4 Failure modes and influence of experimental variables

3.4.1 Failure modes

Four failure modes were observed in this study: panel flexural failure, panel pull-over, screw fracture and/or plastic bending and girt failure (see Table 3.2). The panel flexural failure mode was observed in Test#1 only, because the panel was reinforced at the midspan in all other tests. A panel pull-over failure was observed in the 203 mm deep members (t=2.54mm) without rigid board insulation. The locally stocky cross-section rotated as a rigid body as the shear flow in the free flange increased, prying the fastener head through the panel. The 203 mm deep member failure mode changed to girt yielding as rigid board thickness increased because the thick rigid board worked like a washer to distribute the force from the screw head across the panel. Screw fracture and/or plastic bending (see Fig. 3.8) were also observed in the 203 mm deep members, especially with thicker rigid board insulation, because the insulation between the through-fastened girt flange and panel could not resist the concentrated moment on the fasteners as the girt rotated as a rigid body. This failure mode was not observed in the 254 mm deep members because the flange was not thick enough (t=1.52 mm) to develop a moment on the fastener. All 254 mm deep members experienced girt failure (see Fig. 3.9) because the cross-section deformed and rotated at the web-flange intersection (instead of rotating as a

rigid body for the thicker girts). In this case the through-fastened connection and rigid board insulation had a minimal influence on girt behavior.

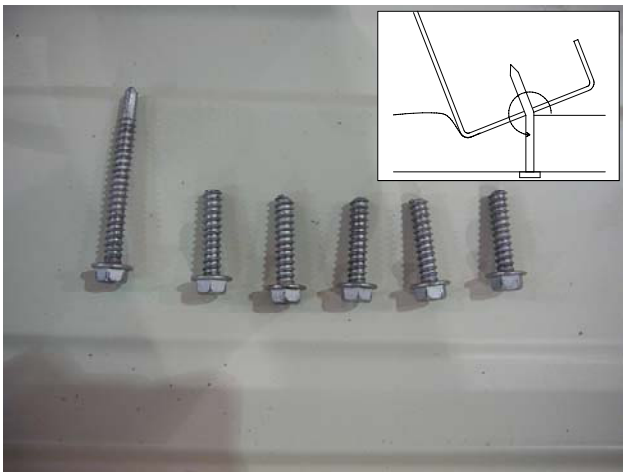

Fig. 3.8 Fractured and bent fasteners (Test#16: Z200D-TH25-1).

Fig. 3.9 Girt failure at girt midspan (Test#28: Z250D-TH25-2).

3.4.2 Effect of screw location

During the tests, it was observed that girt capacity is very sensitive to the screw location *c* [16]. For example, in Fig. 10, when *c* decreased from 53mm to 28mm for the same specimen type (Z200, panel-D, 101.6mm Thermax) the maximum pressure at failure decreased by 30%. Also, larger girt rotation (Fig. 3.11) was observed in the test with *c*=28mm, because smaller *c* provides a lower rotational restraint [16].

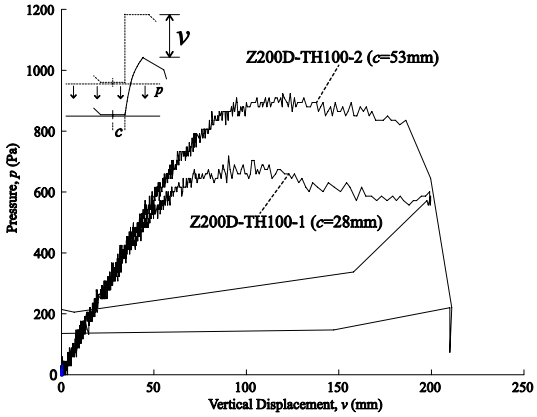

Fig. 3.10 Effect of screw location *c* on the girt load-vertical displacement response

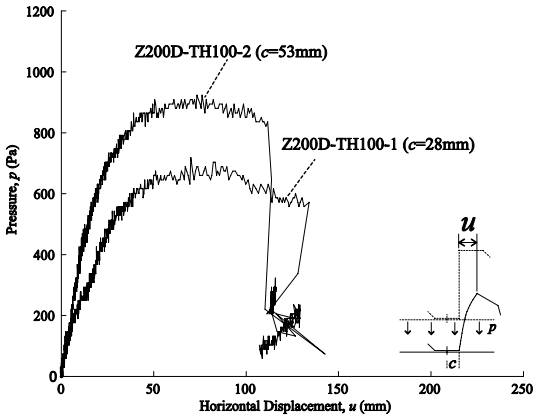

Fig. 3.11 Effect of screw location *c* on the girt load-horizontal displacement response

3.4.3 R-factors

The AISI S100-07 prediction equations assume that screw fasteners are placed in the middle of the flange, and therefore the R-factor is consistent with $c=B/2$, where B is the flange width. However, during the experiments, it was very difficult to guarantee that the screws were always placed in the middle of the flange (see Table 3.2 and Table 3.3). To compare the results from different groups and the existing AISI S100-07 R-factors, a normalization was performed to shift all the experimentally derived R-factors in this study to $c= B/2$ as illustrated in Fig. 3.12. Two data points ($[c_1, R_1]$, $[c_2, R_2]$) are defined for each specimen type, and their average is (c_a, R_a) (see Table 3.2). The R-factor for

$c=B/2$, R^*, is then calculated with the linear interpolation $R^*=R_a+m(B/2-c_a)$. The parameter m is calculated in [16] and reported in Table 3.2.

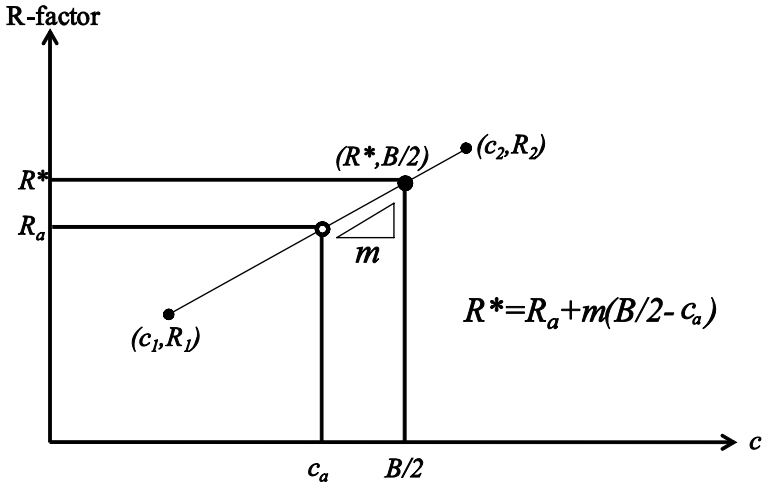

Fig. 3.12 R-factor normalization scheme.

R-factor bare panel trends for Z-section specimens

The girt capacity trends and failure mode (the number on the column, see Table 3.2) for the Z-sections using the bare panel only are summarized in Fig. 3.13. (R-factors discussed in this section and in the sections to follow have been normalized to *c=B/2.*) R-factors for the Z200 girts (203mm deep, 2.54mm thick) are approximately 25% lower than the current AISI R-factor of 0.65 for 165 mm to 216 mm deep Z-sections, resulting from the panel pull-over failure mode initiated by a combination of the relatively thin 0.46mm panel and a rigid locally stocky cross-section. Adding 101.6 mm of compressible fiberglass insulation resulted in a 4% reduction in the R-factor (see specimen Z200D-R100 in Fig. 3.13). The R-factor for the test series Z200B is higher than Z200D because the Bigbee panel had a deeper rib and a higher yield stress that increased the panel pull-over strength. The R-factor for test series Z200BW (Bigbee panel, fastener with washer) is higher than Z200B because the washer improved the panel pull-over strength. Tested Z250 girt (254mm deep, 1.52mm thick) R-factors are consistent with the current AISI R-

factor of 0.50. Remember, all of these locally slender members failed in local buckling. This is why the girt capacity was not sensitive to panel type (compare Z250D to Z250B in Fig. 3.13).

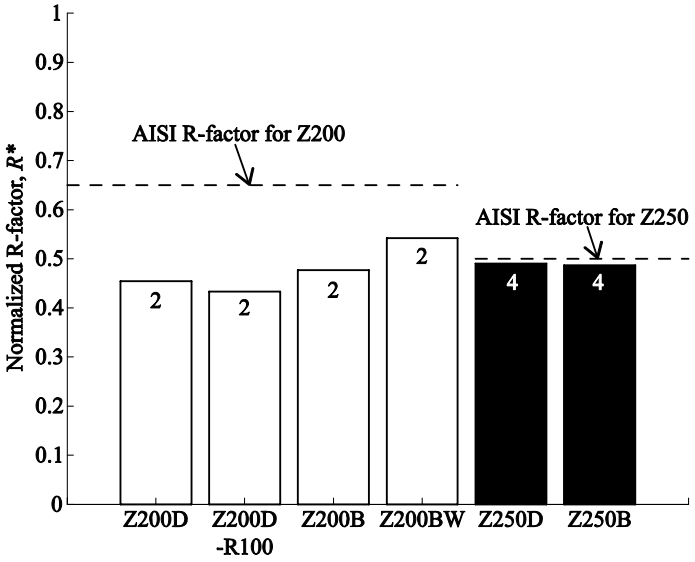

Fig. 3.13 R-factors of Z-sections using bare panel (failure mode type is show at the top of each bar)

Effect of rigid board thickness

For the stocky cross-section Z200 and C200 tests (see Fig. 3.14 and Fig. 3.15), the rigid board prevented panel pull-over (failure mode 2) because of the "washer effect" (see Fig. 3.2), however, at the same time, induce a lower rotational restraint [16] and fractured and/or bent screws (failure mode 3). The rigid board causes some combined failures as well (e.g., Z200-TH250) and a change of failure mode from panel pull-over to girt failure. The R-factor is reduced from 0.65 (in current AISI) to about 0.5 (see Fig. 3.14) and 0.4 (see Fig. 3.15) for Z200 and C200 respectively by adding the rigid board. Notice that the failure mode 3 (screw bending/fracture) is prevented in test Z200-TH100 (see Fig. 3.14) by using a larger screw diameter (#1/4-14), however the R-factor is still lower than 0.65 because of the lower rotational restraint caused by the presence of the

rigid board insulation. Z250 and C250 specimens consistently failed in local buckling, and the R-factor (0.5 for Z-section in Fig. 3.14, 0.4 for C-section in Fig. 3.15) is not reduced by adding rigid board insluation.

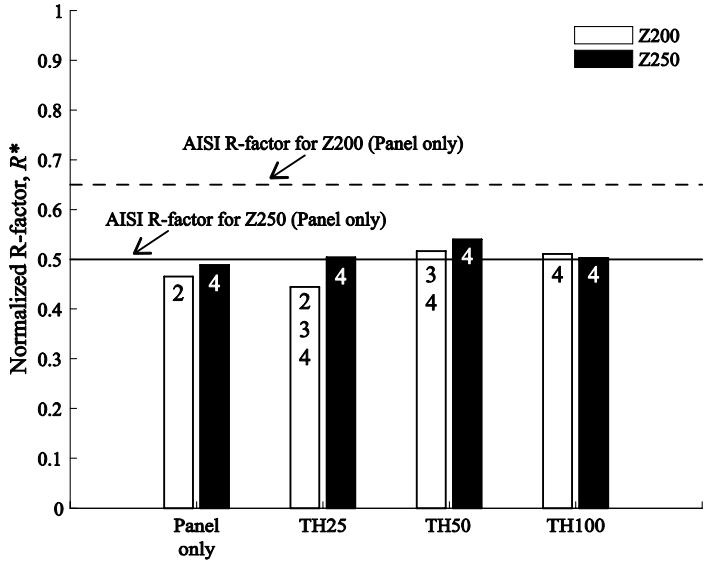

Fig. 3.14 Influence of rigid board on R-factors for Z-sections (failure mode type is show at the top of each bar)

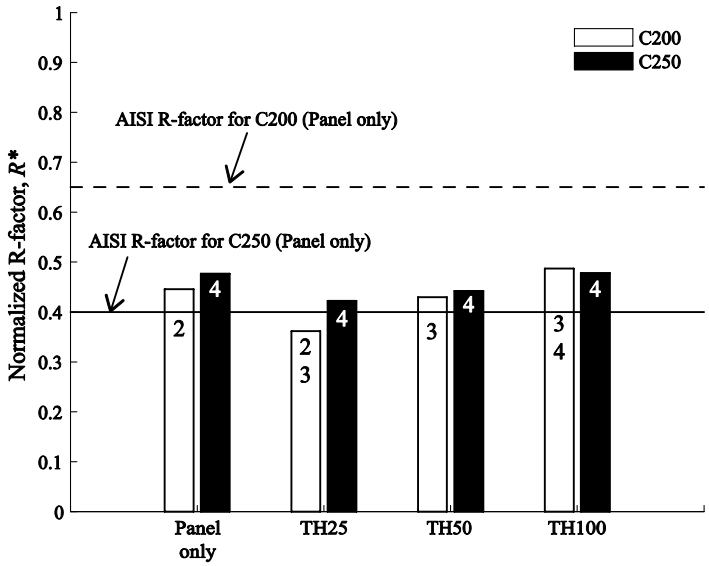

Fig. 3.15 Influence of rigid board on R-factors for C-sections (failure mode type is show at the top of each bar)

3.5 Conclusions

Vacuum box experiments were conducted to observe and quantify the influence of rigid board insulation on girt capacity in metal building wall systems. Four failure limit states were observed: panel flexural failure, panel pull-over (for bare panel), screw fracture and/or plastic bending (for rigid insulation) and girt failure. Girt capacity was not influenced by the presence of rigid board insulation when the cross-section slenderness was high (254mm deep, 1.52mm thick) because the failure mode was dominated by local buckling in the cross-section. For the locally stocky cross-sections (203mm deep and 2.54mm thick), girt capacity was reduced by rigid board insulation because of the lower rotational restraint and screw bending and fracture. Panel pull-over was the dominant limit state for tests without insulation, resulting in lower R-factors when compared to those currently specified by the AISI specification. Girt capacity is sensitive to screw location in the through-fastened flange because rotational restraint provided to the girt from the wall varies with screw location.

References

[1] Winter G, Lansing W, McCalley RB. Performance of laterally loaded channel beams. Engineering Structures Supplement, Colston Papers 1949; 2, 179-190.
[2] Zetlin L, Winter G. Unsymmetrical bending of beams with and without lateral bracing. ASCE Journal of Structural Division 1955; 81, 774-1.
[3] Gao T, Moen CD. Direct strength flexural capacity prediction of through-fastened cold-formed steel roof purlins and wall girt system wind uplift or suction. In: 21st International Specialty Conference on Cold-Formed Steel Structures, St. Louis, Missouri; 2012.
[4] LaBoube RA. Roof panel to purlin connections: rotational restraint factor. In: IABSE Colloquium on Thin-Walled Metal Structures in Buildings, Stockholm, Sweden; 1986.
[5] Rousch CJ, Hancock GJ. Purlin-sheeting connection tests. Research report R724, School of Civil and Mining Engineering, The University of Sydney, Australia; 1996.
[6] Gao T, Moen CD. Predicting rotational restraint provided to wall girts and roof purlins by through-fastened metal panels. Thin-Walled Structures; 2012.

[7] Gao T, Moen CD. Prediction of flexural capacity of through-fastened metal building wall girts and roof purlins with rigid insulation. Journal of Constructional Steel Research; 2012.
[8] AISI-S100. North American Specification for the Design of Cold-Formed Steel Structural Members. Washington, D.C.: American Iron and Steel Institute; 2007.
[9] AS/NZS-4600. Australian/New Zealand Standard: Cold-formed Steel Structures; 2005
[10] EN-1993. Eurocode 3: Design of Steel Structures. European Committee for Standardization, Brussels, Belgium; 2006.
[11] Pekoz T, Soroushian P. Behavior of C- and Z-Purlins under wind uplift. In: Sixth International Specialty Conference on Cold-Formed Steel Structures, Rollar, Missouri; 1982.
[12] ASHRAE-90.1. ASHRAE Standard: Energy standard for buildings except low-Rise residential buildings. American Society of Heating, Refrigerating and Air-Conditioning Engineers, Inc., Atlanta, Georgia; 2010.
[13] Wilsea M, Johnson KL, Ashby MF. Indentation of foamed plastics. International Journal of Mechanical Sciences 1975; 17, 457-460.
[14] Flores-Johnson EA, Li QM. Indentation into polymeric foams 2010; 47, 1987-1995.
[15] MBMA. Summary of interior and exterior fire wall mock-ups, MBMA Bulletin No. 145-09(E). Metal Building Manufacturers Association, Cleveland, Ohio; 2009.
[16] Gao T, Moen CD. Experimental evaluation of a vehicular access door subjected to hurricane force wind pressures. Virginia Tech Research Report, Blacksburg, Virginia; 2009.
[17] US Department of Energy. The R-Value of Insulation; 2008. <http://www.energysavers.gov/your_home/insulation_airsealing/index.cfm/mytopic=11340>
[18] Fisher JM. Uplift capacity of simple span Cee and Zee members with through-fastened roof panels. Report for Metal Building Manufacturers Association, Cleveland, Ohio; 1996.
[19] ASTM E8M. Standard test methods for tension testing of metallic materials; 2000.
[20] Gao T, Moen CD. Flexural strength of exterior metal building wall assemblies with rigid insulation. Virginia Tech Research Report No. CE/VPI-ST-11/01, Blacksburg, Virginia; 2011.
[21] Gao T, Moen CD. "Test videos-flexural strength experiments on exterior metal building wall assemblies with rigid insulation." 2012. Virginia Tech, Blacksburg, VA. <http://hdl.handle.net/10919/18714>.
[22] RSG. Cold-Formed Steel Design Software. [Computer software]. RSG Software, Inc.; 2007. <http://www.rsgsoftware.com/>.

Chapter 4: Metal Building Wall and Roof System Design using the Direct Strength Method – Through-Fastened Simple Span Girts and Purlins with Laterally Unbraced Compression Flanges

*(*Submitted to *ASCE Journal of Structural Engineering)*

"Metal Building Wall and Roof System Design using the Direct Strength Method – Through-Fastened Simple Span Girts and Purlins with Laterally Unbraced Compression Flanges"

Abstract

A Direct Strength Method (DSM) prediction approach is introduced and validated for metal building wall and roof systems constructed with steel panels through-fastened with screws to girts or purlins. The focus is capacity prediction for simple spans under wind uplift or suction, however the DSM framework is generally formulated to accommodate gravity loads, continuous spans, standing seam roofs, and insulated roof and wall systems in the future. System flexural capacity is calculated with the usual DSM approach – global buckling, local-global buckling interaction, and distortional buckling strengths are determined with a finite strip eigen-buckling analysis including a rotational spring that simulates restraint provided by the through-fastened steel panel. The DSM flexural capacity is then reduced with a code-friendly equation consistent with existing Eurocode provisions to account for the additional stress at the intersection of the web and free flange that occurs as the girt or purlin rotates under a suction (uplift) load. A database of 62 simple span tests was assembled to evaluate strength prediction accuracy of the proposed DSM approach alongside existing Eurocode and American Iron and Steel Institute (AISI) provisions. The proposed DSM approach is confirmed to be viable and accurate for simple spans. Modifications to the Eurocode approach are proposed, and if they are made, the Eurocode is also an accurate and potentially general prediction method. The AISI R-factor prediction method is accurate for C-section simple spans, unconservative for Z-section simple spans, and overall lacks the generality of the DSM and Eurocode.

4.1 Introduction

This paper presents a system capacity prediction method for metal building wall and roof systems constructed with cold-formed steel girts or purlins through-fastened to steel panels. For these systems, uplift or suction loading from wind places a girt or purlin's free unbraced flange in compression as shown for C- and Z-sections in Fig. 4.1. Member failure initiates at the midspan intersection of the web and free flange from a combination of restrained lateral-torsional buckling deformation and cross-section distortion and rotation caused by strong-axis flexure-induced shear flow [1-3]. The cross-section center of twist, treated as the shear center for C- and Z-sections on their own [4], changes locations when a girt or purlin is through-fastened to a metal panel (see Fig. 4.1) which has implications for flexural strength prediction that will be discussed herein.

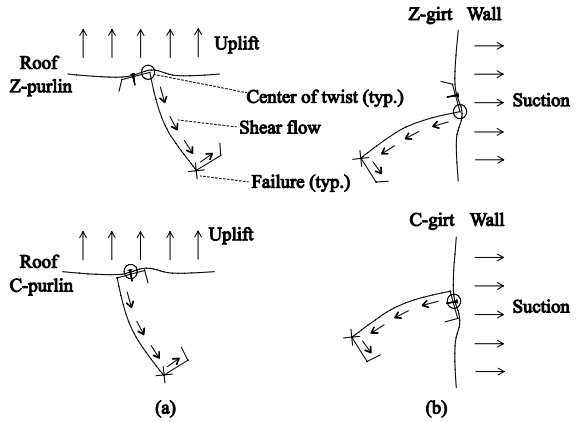

Fig. 4.1 (a) Purlin with wind uplift loading; (b) girt with wind suction loading

Through-fastened wall and roof system design approaches are semi-analytical in Europe and experimentally based in North America, Australia, and New Zealand. The European approach [5] is motivated by a mechanics-based model by Zetlin and Winter [2] and strength prediction approaches by Douty [6] and Peköz and Soroushian [7] which were validated experimentally (e.g., LaBoube [8]) and with computational simulations (e.g., Rousch and Hancock [9]). Widespread use of the Eurocode approach is limited

though because of the perceived complexity of the analysis method and because the rotational restraint provided by the metal panel to the cross-section, an important part of a wall or roof system strength prediction procedure, could historically only be quantified by conducting experiments [10-11].

In North America, Australia, and New Zealand [12-13], wall and roof system wind uplift (suction) capacity prediction is calculated with an experimentally derived knock down factor, i.e., the R-factor, applied to the nominal flexural capacity [14]. The R-factor decreases with increasing cross-section depth and is applicable within prequalified ranges of cross-section dimensions and metal panel thicknesses.

Recent research has demonstrated that the R-factor approach may not be accurate for cases where other limit states govern system strength [15], for example, fasteners pulling through the metal panels as the girt or purlin deforms under load. Also, the R-factor approach cannot accommodate other types of wall panel configurations, for example, when rigid board insulation is sandwiched between the wall panel and through-fastened flange.

The goal of this paper is to propose a general system strength approach for metal building wall and roof systems that leverages recent advances in cold-formed steel design through the Direct Strength Method (DSM) [12]. The work presented here focuses on capacity prediction for wind suction (uplift) and simple span girts and purlins, however the ideas and framework are general and can accommodate other limits states and continuous spans in the future. Accuracy of the three strength prediction approaches – R-factor method (AISI and AS/NZS), Eurocode, and the DSM – is evaluated with a database of 62 tests compiled by the first author. An introduction to the three prediction

methods is presented in the next section. Dimension notation used in this paper is provided in Fig. 4.2.

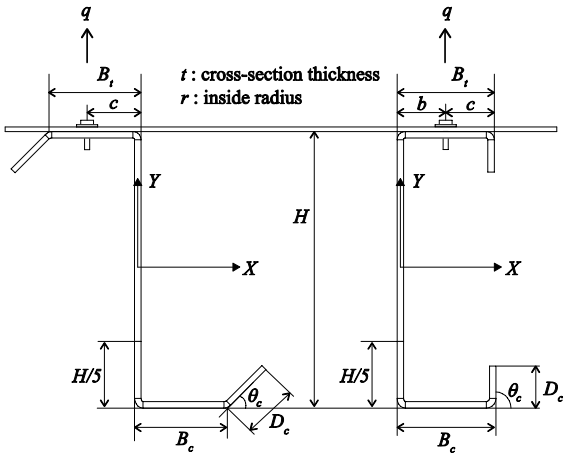

Fig. 4.2 Cross-section dimension notation

4.2 R-factor prediction method

Current AISI and AS/NZS prediction methods employ experimentally derived R-factors. In the R-factor method, $M_n=RS_eF_y$, where S_e is the effective section modulus of the cross-section calculated relative to the extreme compression or tension fiber about the centroidal strong axis, i.e., the X-axis in Fig. 4.2, and F_y is the steel yield stress. The R-factor varies with web depth as shown in Table 4.1. AS/NZS recommends the use of AISI R-factors for the case when cyclone washers are not used with the fasteners, which is the case assumed in this paper.

Table 4.1 R-factor (AISI and AS/NZS)

Web depth, mm	Profile	R
$H \leq 165$	C or Z	0.70
$165 < H \leq 216$	C or Z	0.65
$216 < H \leq 292$	Z	0.50
$216 < H \leq 292$	C	0.40

4.3 Eurocode prediction method

The Eurocode prediction method [5] isolates the compressed free girt or purlin flange and a partial web section ($H/5$) from the cross-section (Fig. 4.3a) and treats it as a beam on an elastic foundation (Fig. 4.3b). The lateral force w (force/length) represents the shear flow in the compressed flange from strong axis flexure (see Fig. 4.1) and the foundation spring K (stiffness/length) simulates lateral restraint provided by the web and the through-fastened connection.

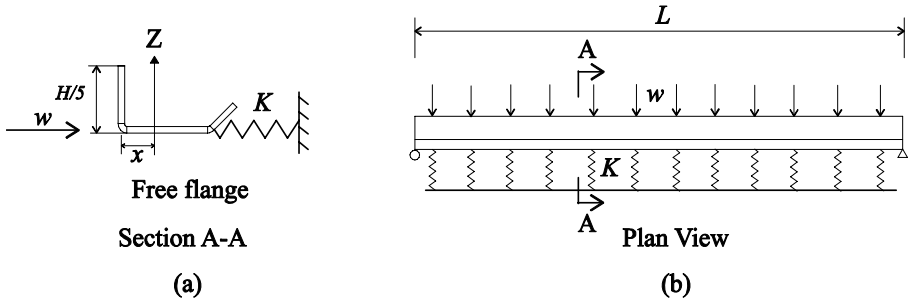

Fig. 4.3 (a) Isolated free flange and partial web; (b) beam on an elastic foundation

Prediction model and interaction equation

The failure stress at the intersection of web and free flange results from a combination of lateral-torsional buckling deformation, i.e., the first term in Eq. (4.1), and the stress from lateral deformation of the free flange caused by shear flow (σ_f)

$$\frac{1}{\chi_{LT}} \cdot \frac{M_x}{S_e} + \sigma_f \leq F_y \tag{4.1}$$

where

$$\sigma_f = \frac{M_f}{S_f}. \tag{4.2}$$

The moment M_x is the required purlin or girt moment capacity and χ_{LT} is the reduction factor for lateral-torsional buckling deformation calculated using European

buckling curve-b. The bending moment in the free flange caused by shear flow is approximated as

$$M_f = k_R \frac{wL^2}{8}. \tag{4.3}$$

The factor k_R accounts for a moment magnitude reduction in the free flange (Fig. 4.3b) from the distributed spring K

$$k_R = \frac{1-0.0225r}{1+1.013r}, \tag{4.4}$$

where

$$r = \frac{KL^4}{\pi^4 EI_f} \tag{4.5}$$

and the flange centroidal strong axis (Z-axis in Fig. 4.3a) moment of inertia is

$$I_f = \left(\frac{Ht^3}{60} + \frac{Htx^2}{5}\right) + \left[\frac{tB_c^{\,3}}{12} + B_c t\left(\frac{B_c}{2} - x\right)^2\right] + \left[\cos^2(\theta_c)\frac{tD_c^{\,2}}{12} + D_c t(B_c + \frac{\cos(\theta_c)D_c}{2} - x)^2\right]. \tag{4.6}$$

The origin of Eq. (4.4) is not documented in Eurocode, however it was established through personal communication [16] that it is an approximation of an exact solution. The authors of this paper confirmed the equation's accuracy with a computer structural analysis parameter study [17].

The gross section modulus of the partial web and the free flange, S_f, about the Z-axis in Fig. 4.3a to the compression extreme fiber is

$$S_f = \frac{I_f}{x} \tag{4.7}$$

where the distance from the centroid to the extreme fiber in compression, x, is

$$x = \frac{B_c^{\,2}/2 + B_c D_c + D_c^{\,2}\cos(\theta_c)/2}{H/5 + B_c + D_c}. \tag{4.8}$$

Equivalent shear flow calculation

The Eurocode calculates the lateral force w for a C-section by assuming the cross-section is a frame with a fixed restraint provided by the panel beyond the fastener as shown in Figure 4a, where the moment reaction $M_r=sH+qb$, and $s=qB_ctH^2/(4I_x)$ is the shear flow magnitude in the free flange [7]. An equivalent force per length w in the free flange is derived by assuming $M_r=wH$. Solving for w results in

$$w = qk_H \quad , \quad k_H = (B_c tH^2/4I_x + b)/H \quad , \tag{4.9}$$

where q is the uplift (suction) distributed load (force/length) on a purlin or girt, and I_x is the moment of inertia of the cross-section about the X-axis in Fig. 4.2. The out-to-out web depth is H, base metal thickness is t, the free (compressed) flange width is B_c, and lip stiffener length is D_c as shown in Fig. 4.2.

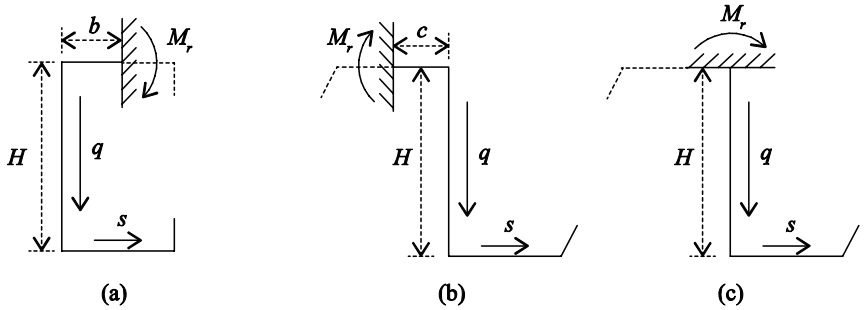

Fig. 4.4 Assumed through-fastened fixity for (a) C-section in Eq. (4.9); (b) Z-section in Eq. (4.10); (c) Z-section in Eq. (4.11)

The Eurocode calculation of the lateral force w for a Z-section in restrained strong axis bending is established with a similar approach to a C-section as shown in Fig. 4.4b. The moment reaction provided by the through-fastened panel is $M_r=sH-qc$ which is

assumed equivalent to M_r=wH, resulting in

$$w = qk_H \quad , \quad k_H = \frac{Ht(B_c^{\,2} + 2D_cB_c - 2D_c^{\,2}B_c / H)}{4I_x} - \frac{c}{H}. \tag{4.10}$$

A question arises with this derivation though. The fixity location in Fig. 4.4b is not consistent with observed behavior (e.g. [7, 15 and 18]). The cross-section center of rotation is more likely at the web-flange intersection as shown in Fig. 4.4c. For this case, M_r=sH resulting in

$$k_H = \frac{Ht(B_c^2 + 2D_cB_c - 2D_c^2B_c / H)}{4I_x} \tag{4.11}$$

This modification to Eq. (4.10) removes the possibility of negative values for w discussed in the Eurocode. (A negative value can occur because for some cross-sections the rotation from shear flow in the web dominates over the opposite rotation from shear flow in the flange.) Strength predictions with both approaches, i.e., the use of Eq. (4.10) vs. Eq. (4.11), will be compared to test results later in the paper.

Equivalent rotational stiffness calculation

The distributed spring stiffness K has in the past been calculated with empirically derived equations [5] or obtained from tests [10-11], however for this study K is calculated with recently derived rotational restraint engineering expressions presented in Gao and Moen [19].

The stiffness K is obtained by dividing the equivalent shear flow force, w, by the lateral deflection caused by (1) rigid body rotation of the cross-section restrained by the through fastened connection (Δ_1); and (2) cantilever bending of the web about the tension flange-web intersection (Δ_2) as shown in Fig. 4.5.

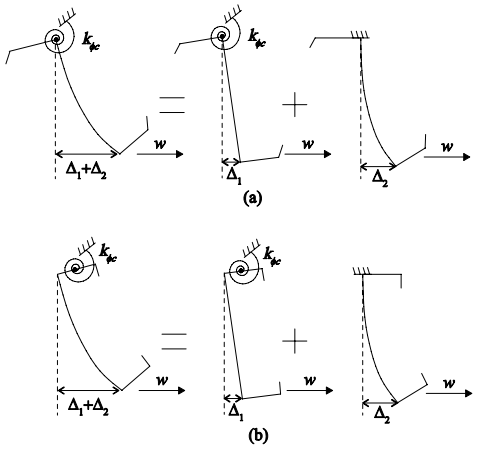

Fig. 4.5 Stiffness *K* calculation for a (a) Z-section (b) C-section

The equation for K is

$$K = \frac{w}{\Delta_1 + \Delta_2} \tag{4.12}$$

where

$$\Delta_1 = \frac{wH}{k_{\phi c}} \cdot H \tag{4.13}$$

and

$$\Delta_2 = \frac{wH^3}{3EI} \ . \tag{4.14}$$

The girt or purlin modulus of elasticity is E, $I=t^3/12$ is the unit web bending stiffness treated as a cantilever, and the distributed rotational stiffness k_c is calculated as [19]

$$k_{\phi c} = \left(\frac{S}{c^2 k_p} + \frac{c}{3EI} \right)^{-1} , \tag{4.15}$$

where S is the fastener spacing and k_p is the panel pull-out stiffness at each fastener calculated with finite element analysis of the panel [17]. Note that k_p can be tabulated for standard panel cross-sections and fastener locations as discussed in Gao and Moen [19].

The rotational stiffness in Eq. (4.15) was originally derived for Z-sections, however it is also used in this paper for C-sections because the flange bending influence, i.e., the second term in Eq. (4.15), is the same for both Z- and C-sections assuming the C-section through-fastened center of fixity is located as shown in Fig. 4.4a.

The proposed DSM strength prediction approach discussed in the next section merges the Eurocode approach with finite-strip eigenbuckling analysis.

4.4 Proposed DSM prediction method

Prediction model and interaction equation

The DSM strength prediction method for through-fastened girts or purlins in uplift or suction employs the interaction equation

$$\frac{M}{S_c}+\sigma_f \le \frac{M_{ne}}{S_c}\ ,\ \frac{M}{S_c}+\sigma_f \le \frac{M_{n\ell}}{S_c}, \tag{4.16}$$

where M is the required flexural strength, S_c is the gross strong centroidal axis section modulus for the extreme compression fiber, and σ_f is the flange bending stress due to shear flow calculated with Eq. (4.2). This approach assumes that girt or purlin failure occurs as lateral-torsional buckling deformation is amplified near peak load by cross-section rotation and distortion from shear flow [20]. The DSM framework is more consistent with physically observed behavior than the Eurocode approach because it addresses local-global buckling interaction of girts or purlins in the calculation of M_n . Also, the global buckling capacity M_{ne} is calculated including the influence of rotational restraint provided by the through-fastened connection [21].

DSM R-factor derivation for simple span girts and purlins

If M is assumed equal to $R_{DSM}M_{ne}$ for global buckling deformation (or $M=R_{DSM}M_n$. for local-global buckling interaction) where R_{DSM} is a reduction factor that

accounts for cross-section deformation from shear flow, then Eqs. (4.16) can be rewritten as equalities

$$\frac{R_{DSM}M_{ne}}{S_c}=\frac{M_{ne}}{S_c}-\sigma_f,\ \frac{R_{DSM}M_{n\ell}}{S_c}=\frac{M_{n\ell}}{S_c}-\sigma_f. \tag{4.17}$$

For the specific case considered in this paper – simple span C- and Z-sections, M_f is expanded by substituting $w=qk_H$ into Eq. (4.3)

$$M_f=k_Rk_H\frac{qL^2}{8}. \tag{4.18}$$

And since $R_{DSM}M_{ne}=qL^2/8$ (or $R_{DSM}M_n=qL^2/8$), then

$$M_f=k_Rk_HR_{DSM}M_{ne},\ M_f=k_Rk_HR_{DSM}M_{n\ell}. \tag{4.19}$$

A simple span R_{DSM} factor equation is obtained by substituting Eq. (4.2) and Eqs. (4.19) into Eqs. (4.17), resulting in

$$R_{DSM}=\left(1+\frac{S_c}{S_f}k_Hk_R\right)^{-1}. \tag{4.20}$$

The flow of a typical DSM calculation is thus preserved in the proposed approach where $M_n=\min(R_{DSM}M_{ne},\ R_{DSM}M_n,\ M_{nd})$. It is assumed that the distortional buckling limit state is not influenced by shear flow and therefore M_{nd} is not multiplied by R_{DSM}. The stress gradient in the compression flange caused by lateral bending from shear flow minimizes the distortional buckling influence.

DSM implementation details – finite strip analysis including rotational restraint

When calculating M_{ne} and $M_{n\ell}$ from M_{cre} and $M_{cr\ell}$ using finite strip eigen-buckling analysis [22] the rotational restraint provided by the metal panel to the member's through-fastened flange is simulated by adding a roller and a rotational spring

(see Fig. 4.6a) at the cross-section's center of twist (see Fig. 4.1). The rotational spring stiffness is calculated with Eq. (4.15). The location of the spring in the finite strip analysis should coincide with the cross-section's center of twist when through-fastened to the panel, see Fig. 4.1. The reference stress in the finite strip analysis is calculated assuming restrained bending about the strong centroidal axis as shown in Fig. 4.6b. The critical elastic global buckling moment M_{cre} is multiplied by a moment gradient factor C_b=1.13 to account for the parabolic moment diagram in a simple span.

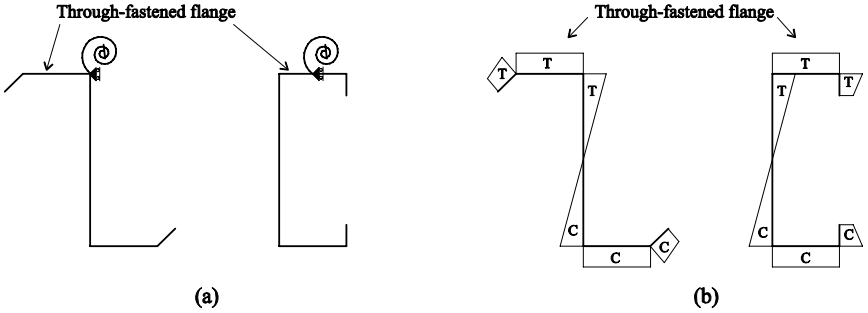

Fig. 4.6 (a) Lateral and rotational restraint; and (b) longitudinal reference stress in a finite strip eigen-buckling analysis

4.5 Experimental database

Previous literature was reviewed to collect 62 tested strength data points from 7 simple span pressure box experimental programs as shown in Table 4.2. All experiments consisted of two parallel C- or Z-section members through-fastened to steel sheeting. The member cross-section dimensions (see Fig. 4.2 for notation), span lengths, steel yield stress, calculated rotational spring stiffness, and tested flexural capacity are summarized in Table 4.4-4.7.

Table 4.2 Experimental program summary

Series	Year	Profile C	Profile Z	Panel Thickness (mm)	Panel Rib Depth (mm)	Fastener Location	Imperfection	Boundary Condition
S1	Pekőz and Soroushian (1982)	3	13	0.56	38	Middle	Available	Pin-roller
S2	LaBoube (1983)	4	5	0.46	38	Middle	Available	Bolted
S3	LaBoube and Golovin (1990)	1	1	0.46	38	Middle	N/A	Bolted
S4	Hancock (1990)	1	1	0.42	29	Crest	N/A	Pin-roller
S5	Rousch and Hancock (1997)	1	1	0.42	29	Crest	N/A	Pin-roller
S6	Fisher (1996)	5	20	0.46	38	Next	N/A	Pin-roller
S7	Gao and Moen (2012a)	2	4	0.46	29	Next	Available	Pin-roller

Fasteners were centered between primary ribs in test series S1 to S3 (Middle), at the primary ribs in S4 and S5 (Crest), and next to the primary ribs in S6 and S7 (Next). The imperfection magnitudes were assumed as zero if not provided. There was no catenary action in test series S1 and S4 to S7 because pin-roller boundary conditions were used. (Pin-roller boundary conditions are consistent with the Eurocode approach and the proposed DSM method). Catenary action was most likely present in test series S2 and S3 because the member tension flange was bolted to both supports. The focus in the studies of LaBoube and Golovin [23], Hancock [24] and Rousch and Hancock [9] were the continuous span and the effect of bridging, and there were only two simple span tests.

The fastener location in the flange, i.e., b and c in Fig. 4.2, were measured in test series S7 (and also used when predicting capacity in the following section) because both rotational restraint [19] and flexural strength [25] are functions of these dimensions. In test series S1 to S6, it is assumed that the fastener is placed at the center of the flange ($b=c=B_f/2$ in Figure 2). The fastener spacing (S) for all test series was 305mm, and the local panel-fastener stiffness k_p is calculated with second order elastic finite element analysis (see Table 4.5).

4.6 Test-to-predicted comparisons

The average (MEAN), coefficient of variation (COV), and LRFD resistance factor ( ) calculated with AISI-S100 Chapter F (AISI 2007) (β=2.5) are summarized in Table

4.3 for each of the prediction methods. Elastic buckling and DSM prediction parameters are listed in Table 4.5 and 4.6. The test-to-predicted flexural capacity ratio for each test in the simple span database is provided in Table 4.7.

Table 4.3 Test-to-predicted statistics

M_{test}/M_n									
Prediction	C-section (n=17)			Z-section (n=45)			C- and Z-section (n=62)		
Method	MEAN	COV	ϕ	MEAN	COV	ϕ	MEAN	COV	ϕ
R-factor	1.04	0.15	0.90	0.91	0.18	0.78	0.95	0.18	0.81
Euro Eq. (10)	1.08	0.19	0.91	0.89	0.20	0.75	0.95	0.22	0.79
Euro Eq. (11)	1.08	0.19	0.91	0.96	0.17	0.82	0.99	0.19	0.85
DSM	1.12	0.18	0.95	1.02	0.17	0.88	1.05	0.18	0.90

The R-factor method produces the most accurate strength predictions for C-sections (mean of 1.04 and COV of 0.15), however it is unconservative for Z-sections (mean of 0.91 and COV of 0.18). Considering the complete test database, the R-factor method has an LRFD resistance factor of 0.81 which is lower than Φ=0.90 current specified in AISI-S100-07 for flexural members.

The Eurocode approach using Eq. (4.10) is accurate for C-sections (mean of 1.08 and COV 0.91) but it makes unconservative predictions for Z-sections (mean of 0.89 and COV of 0.20). When using Eq. (4.11) instead for the Z-section predictions (which removes the web shear flow influence), the test-to-predicted statistics improve both for Z-sections (mean of 0.96 and COV of 0.17) and across the complete database (mean and COV are 0.99 and 0.19). Our findings suggest that the Eurocode prediction accuracy could be improved by replacing Eq. (4.10) with Eq. (4.11).

The DSM is also a viable strength prediction approach as demonstrated by the test to predicted mean of 1.05 and a COV of 0.18. The test-to-predicted statistics result in an LRFD resistance factor of ϕ=0.90 consistent with the current AISI specification.

Table 4.4 Specimen cross-section dimensions and yield stress

Test #	Profile	D_c (mm)	B_c (mm)	θ_c (deg.)	H (mm)	D_t (mm)	B_t (mm)	θ_t (deg.)	r (mm)	t (mm)	F_y (MPa)
S1-1	Z	32.0	82.2	36	203.2	32.0	82.2	36	14.7	1.50	455
S1-2	Z	25.4	69.3	40	201.2	25.4	69.3	40	7.6	1.52	424
S1-3	Z	24.0	69.7	50	204.6	24.0	69.7	50	7.1	1.60	393
S1-4	Z	34.6	78.0	40	202.4	34.6	78.0	40	13.4	1.78	446
S1-5	Z	34.5	79.8	41	203.2	34.5	79.8	41	14.0	1.91	446
S1-6	Z	32.4	77.5	41	204.0	32.4	77.5	41	11.7	2.24	440
S1-7	Z	35.2	79.0	43	203.2	35.2	79.0	43	12.6	2.26	442
S1-8	Z	30.4	73.6	48	201.7	30.4	73.6	48	7.8	2.90	387
S1-9	Z	34.8	75.7	36	201.4	34.8	75.7	36	11.3	2.92	455
S1-10	Z	34.0	78.0	46	244.5	34.0	78.0	46	10.2	1.57	396
S1-11	Z	25.1	71.3	42	240.0	25.1	71.3	42	8.3	1.60	395
S1-12	Z	27.3	78.4	41	243.3	27.3	78.4	41	9.3	2.69	365
S1-13	Z	34.3	74.1	40	241.0	34.3	74.1	40	8.6	2.77	397
S1-14	C	21.3	66.5	90	177.8	21.3	66.5	90	10.3	1.91	380
S1-15	C	21.0	63.8	90	228.6	21.0	63.8	90	7.8	1.91	381
S1-16	C	20.7	66.3	90	228.6	20.7	66.3	90	8.1	1.96	381
S2-1	C	19.1	71.4	90	242.8	20.6	71.4	90	8.0	1.80	445
S2-2	C	20.6	71.4	90	241.3	20.6	69.9	90	8.0	1.80	445
S2-3	Z	22.4	69.9	90	241.3	22.4	71.4	90	8.0	1.80	445
S2-4	Z	20.6	69.9	90	241.3	20.6	69.9	90	8.0	1.80	445
S2-5	Z	19.1	71.4	90	244.6	20.6	69.9	90	8.0	1.80	445
S2-6	C	20.6	71.4	90	241.3	20.6	71.4	90	8.0	2.69	445
S2-7	C	20.6	73.2	90	242.8	20.6	71.4	90	8.0	2.69	445
S2-8	Z	20.6	73.2	90	239.8	20.6	71.4	90	8.0	2.69	445
S2-9	Z	22.4	71.4	90	242.8	20.6	73.2	90	8.0	2.69	445
S3-1	Z	26.9	76.2	77	279.4	31.8	74.7	77	6.4	1.91	425
S3-2	C	22.2	88.9	91	292.1	25.4	88.9	91	6.4	2.24	391
S4-1	Z	20.0	74.0	90	205.0	20.0	83.0	90	4.9	2.45	529
S4-2	C	21.3	77.1	90	206.0	21.3	77.1	90	4.9	2.45	518
S5-1	Z	21.5	72.5	90	202.8	21.5	80.7	90	5.0	1.50	527
S5-2	C	20.8	76.7	90	202.0	20.8	76.7	90	5.0	1.50	548
S6-1	Z	22.9	55.9	51	204.5	26.7	57.2	55	5.2	2.60	405
S6-2	Z	20.3	58.4	54	203.2	25.4	57.2	56	5.2	2.60	407
S6-3	Z	21.6	58.4	52	201.9	25.4	54.6	49	5.2	2.61	408
S6-4	Z	21.6	58.4	50	203.2	26.7	54.6	47	5.2	2.61	406
S6-5	Z	17.8	49.5	47	163.8	15.2	48.3	44	3.1	1.54	411
S6-6	Z	16.5	47.0	43	163.8	17.8	50.8	48	3.1	1.55	422
S6-7	Z	24.1	59.7	51	204.5	24.1	50.8	50	3.0	1.52	437
S6-8	Z	22.9	57.2	49	205.7	25.4	52.1	50	3.6	1.79	400
S6-9	Z	26.7	67.3	43	241.3	27.9	67.3	39	3.3	1.67	431
S6-10	Z	25.4	68.6	49	240.0	27.9	68.6	47	3.7	1.87	420
S6-11	Z	22.9	90.2	38	292.1	21.6	91.4	53	4.2	2.10	386
S6-12	C	20.3	62.2	90	163.8	20.3	63.5	90	3.0	1.52	427
S6-13	C	21.6	62.2	88	163.1	21.6	63.5	87	3.0	1.52	428
S6-14	C	17.8	63.5	93	204.5	21.6	62.2	95	3.1	1.53	420
S6-15	C	17.8	63.5	91	203.2	20.3	63.5	90	3.9	1.93	408
S6-16	Z	16.5	48.3	41	163.8	20.3	48.3	43	4.2	2.10	431
S6-17	C	26.7	62.2	87	162.6	24.1	63.5	88	4.2	2.09	421
S6-18	Z	25.4	68.6	52	200.7	27.9	66.0	48	4.1	2.05	428
S6-19	Z	24.1	68.6	50	200.7	26.7	67.3	51	4.1	2.07	391
S6-20	Z	25.4	66.0	45	200.7	26.7	67.3	50	4.2	2.08	400
S6-21	Z	25.4	68.6	48	200.7	25.4	67.3	48	4.2	2.08	335
S6-22	Z	25.4	68.6	51	200.7	26.7	66.0	50	4.1	2.06	405
S6-23	Z	25.4	68.6	51	200.7	25.4	67.3	47	4.2	2.08	411
S6-24	Z	25.4	68.6	53	200.7	25.4	67.3	49	4.1	2.07	404
S6-25	Z	25.4	68.6	46	200.7	25.4	67.3	48	4.1	2.05	419
S7-1	Z	19.8	71.9	55	254.0	20.3	71.9	46	7.1	1.52	404
S7-2	Z	20.8	71.9	55	254.0	21.3	72.6	48	6.4	1.52	401
S7-3	Z	21.1	71.6	55	254.0	22.1	72.9	47	5.8	1.52	402
S7-4	Z	22.4	70.6	54	254.0	20.3	73.2	47	6.1	1.52	399
S7-5	C	20.8	64.5	90	254.0	19.6	65.5	90	5.6	1.52	423
S7-6	C	20.8	64.0	90	254.0	19.3	65.0	90	5.6	1.52	414

Table 4.5 Span length and finite strip analysis results

Test #	L (mm)	k_p (N/mm)	$k_{\phi c}$ (N-mm/rad/mm)	M_{cr} (kN-mm)	M_{crd} (kN-mm)	M_{cre} (kN-mm)	L_{cre} (mm)
S1-1	6096	257	1061	14332	6684	9050	4064
S1-2	6096	303	972	11468	7358	8239	4064
S1-3	6096	302	1002	12981	9522	8936	4064
S1-4	6096	272	1146	21795	11531	11631	4064
S1-5	6096	266	1199	26989	13457	12900	4064
S1-6	6096	274	1236	39218	18517	15161	4064
S1-7	6096	268	1259	42026	20658	16052	4064
S1-8	6096	288	1232	77922	36979	19104	4064
S1-9	6096	280	1268	31736	N.A.	19343	4064
S1-10	6096	272	1072	12866	11490	10939	4679
S1-11	6096	296	1020	12195	9319	9226	4679
S1-12	6096	271	1295	28932	N.A.	18969	4679
S1-13	6096	286	1235	64890	35355	19886	4679
S1-14	6096	314	1027	24206	17949	10007	3529
S1-15	6096	323	983	20046	20923	9777	4064
S1-16	6096	314	1031	22004	21632	10580	4064
S2-1	6096	214	808	17018	17143	9534	4679
S2-2	6096	219	796	17403	18110	9658	4679
S2-3	6096	214	808	17283	19701	10161	4679
S2-4	6096	219	796	17184	18420	9897	4679
S2-5	6096	219	796	17027	17332	9931	4679
S2-6	6096	214	867	55914	42705	15078	4679
S2-7	6096	214	867	56521	42487	15456	4679
S2-8	6096	214	867	56890	42310	15372	4679
S2-9	6096	208	882	56441	45784	15506	4679
S3-1	9144	202	843	19638	24121	12658	5387
S3-2	9144	152	917	32000	30818	16832	6203
S4-1	7000	322	1653	43751	30921	18011	3529
S4-2	7000	326	1471	45254	31395	17839	4064
S5-1	7000	324	1230	10402	11900	9258	4064
S5-2	7000	327	1166	10651	10896	8683	4679
S6-1	5843	412	1066	47339	30048	12262	3529
S6-2	5843	412	1066	28610	N.A.	12276	3529
S6-3	5843	417	991	29069	N.A.	12098	3529
S6-4	5843	417	990	28430	N.A.	12077	3529
S6-5	5843	431	743	10877	7149	5404	3065
S6-6	5843	425	803	10300	6725	5212	2662
S6-7	5843	425	799	10946	9658	7336	4064
S6-8	5843	423	867	16710	13019	8458	3529
S6-9	5843	391	1203	13549	11644	10680	4679
S6-10	5843	388	1299	19120	15846	12612	4679
S6-11	5843	341	1904	25867	15464	19787	5387
S6-12	5843	399	1068	11037	10973	7158	3529
S6-13	5843	399	1069	11160	11348	7290	3529
S6-14	5715	402	1047	10511	11403	7238	4064
S6-15	5715	399	1184	21005	18349	10165	3529
S6-16	7367	431	789	12625	N.A.	6832	2662
S6-17	7367	399	1210	28954	25349	12067	3529
S6-18	7367	394	1273	27032	17846	13299	4064
S6-19	7367	391	1311	27358	16956	13357	3529
S6-20	7367	391	1313	27656	16713	13177	3529
S6-21	7367	391	1313	28395	17246	13624	4064
S6-22	7367	394	1275	27602	17780	13370	4064
S6-23	7367	391	1313	28236	18052	13619	4064
S6-24	7367	391	1311	27838	18429	13564	4064
S6-25	7367	391	1307	27067	16125	13364	4064
S7-1	7468	300	958	9937	8810	8320	4679
S7-2	7468	315	826	9963	9303	8273	4679
S7-3	7468	342	634	9936	9499	7850	4679
S7-4	7468	277	1171	10017	9896	8983	4679
S7-5	7468	372	466	9749	13635	6321	5387
S7-6	7468	326	740	9727	13646	6986	4679

Table 4.6 Test to predicted comparison - DSM

Test #	S_c (mm^3)	S_f (mm^3)	k_R	k_H	R_{DSM}	M_{ne} (kN-mm)	M_{nl} (kN-mm)	M_{nd} (kN-mm)	M_y (kN-mm)	M_n (kN-mm)	M_{test} (kN-mm)	M_{test}/M_n
S1-1	40129	7595	0.27	0.25	0.74	9050	8916	9580	18268	6594	6200	0.94
S1-2	35902	5898	0.17	0.19	0.83	8239	7794	8967	15230	6490	5600	0.86
S1-3	38034	6058	0.17	0.18	0.84	8890	8538	9826	14925	7211	6500	0.90
S1-4	46192	8659	0.23	0.25	0.77	11627	11627	12869	20582	8955	8000	0.89
S1-5	50128	9498	0.23	0.25	0.77	12882	12882	14390	22371	9894	9400	0.95
S1-6	57632	10604	0.21	0.24	0.79	15085	15085	17597	25361	11936	11200	0.94
S1-7	59026	11163	0.22	0.25	0.78	15897	15897	18656	26057	12351	11000	0.89
S1-8	70138	12412	0.19	0.22	0.82	18256	18256	23544	27140	14884	14500	0.97
S1-9	73529	13949	0.22	0.25	0.78	19312	19247	N.A.	33422	15017	12500	0.83
S1-10	52950	8443	0.36	0.18	0.72	10939	9804	12998	20978	7014	8100	1.15
S1-11	48189	7109	0.27	0.15	0.79	9226	8585	11272	19046	6759	7700	1.14
S1-12	86271	13683	0.28	0.17	0.77	18854	18393	N.A.	31478	14130	18100	1.28
S1-13	88172	14239	0.29	0.18	0.75	19877	19877	27414	35031	14977	14800	0.99
S1-14	33107	5542	0.08	0.31	0.87	9090	9090	11066	12559	7931	8600	1.08
S1-15	46557	6245	0.15	0.22	0.80	9777	9777	14664	17742	7844	7900	1.01
S1-16	48622	6696	0.16	0.23	0.79	10572	10572	15262	18529	8368	7000	0.84
S2-1	50938	6958	0.24	0.24	0.71	9534	9534	15934	22651	6769	7100	1.05
S2-2	50400	6991	0.24	0.24	0.71	9658	9658	16162	22412	6870	6800	0.99
S2-3	50921	6883	0.23	0.10	0.85	10161	10161	16787	22644	8628	8400	0.97
S2-4	50072	6815	0.23	0.10	0.85	9897	9897	16200	22266	8429	9200	1.09
S2-5	51121	6994	0.24	0.10	0.84	9931	9931	16037	22733	8389	8200	0.98
S2-6	74063	10439	0.24	0.24	0.71	15078	15078	28108	32934	10685	13400	1.25
S2-7	75281	10793	0.26	0.24	0.70	15456	15456	28366	33476	10792	14300	1.33
S2-8	73971	10699	0.25	0.11	0.84	15372	15372	27998	32894	12835	15900	1.24
S2-9	75675	10589	0.25	0.11	0.84	15506	15506	29179	33652	13024	16500	1.27
S3-1	72526	9447	0.10	0.11	0.93	12658	12391	21957	30815	11506	17700	1.54
S3-2	94906	12936	0.13	0.24	0.81	16832	16832	27041	37116	13663	19500	1.43
S4-1	58775	8847	0.06	0.14	0.95	17980	17980	24198	31081	17095	20100	1.18
S4-2	58798	9405	0.07	0.31	0.88	17791	17791	24010	30446	15568	22200	1.43
S5-1	36356	5291	0.08	0.13	0.93	9258	8175	12479	19153	7624	11300	1.48
S5-2	35919	5632	0.09	0.31	0.85	8683	7888	12245	19677	6666	10400	1.56
S6-1	54226	7674	0.12	0.14	0.90	12262	12262	19074	21955	11021	12500	1.13
S6-2	53659	7700	0.12	0.14	0.90	12274	12274	N.A.	21837	11042	12200	1.10
S6-3	53015	7863	0.13	0.14	0.89	12098	12098	N.A.	21612	10754	11800	1.10
S6-4	53951	7917	0.13	0.14	0.89	12077	12077	N.A.	21881	10706	10400	0.97
S6-5	21485	3238	0.05	0.15	0.95	5358	5358	6374	8833	5114	5300	1.04
S6-6	21765	3053	0.04	0.14	0.97	5209	5209	6375	9173	5033	4900	0.97
S6-7	32443	4892	0.17	0.15	0.86	7336	7094	9581	14187	6083	6100	1.00
S6-8	37905	5455	0.14	0.14	0.88	8458	8458	11187	15164	7458	7800	1.05
S6-9	50510	7112	0.27	0.14	0.79	10680	9809	13362	21775	7763	8300	1.07
S6-10	56157	7903	0.24	0.14	0.81	12612	12257	15847	23589	9927	11200	1.13
S6-11	93333	13388	0.44	0.14	0.70	19787	18348	20188	35986	12800	12800	1.00
S6-12	24502	3841	0.06	0.31	0.89	6905	6823	8300	10461	6072	5600	0.92
S6-13	24615	3885	0.06	0.32	0.89	7008	6916	8442	10543	6141	5900	0.96
S6-14	32974	4495	0.14	0.24	0.80	7238	6939	10059	13851	5577	5600	1.00
S6-15	40784	5670	0.12	0.25	0.83	10083	10083	13444	16653	8345	9900	1.19
S6-16	29077	4270	0.00	0.15	1.00	6832	6832	N.A.	12515	6805	7500	1.10
S6-17	33384	5488	0.01	0.32	0.98	10561	10561	13293	14046	10330	10600	1.03
S6-18	47406	7617	0.05	0.18	0.94	12993	12993	15110	20306	12244	10500	0.86
S6-19	46916	7613	0.05	0.18	0.95	12608	12608	13908	18349	11922	10100	0.85
S6-20	47750	7553	0.05	0.18	0.95	12678	12678	14191	19103	12014	11200	0.93
S6-21	48140	7815	0.05	0.18	0.94	12018	12018	12871	16104	11325	9900	0.87
S6-22	47498	7684	0.05	0.18	0.94	12830	12830	14580	19231	12087	10500	0.87
S6-23	47988	7740	0.05	0.18	0.94	13100	13100	14900	19727	12359	9600	0.78
S6-24	47680	7664	0.05	0.18	0.94	12962	12962	14791	19272	12238	9900	0.81
S6-25	47447	7727	0.06	0.18	0.94	12959	12959	14350	19865	12197	9900	0.81
S7-1	48309	6540	0.14	0.12	0.89	8320	7494	11165	19490	6655	7100	1.07
S7-2	48873	6611	0.15	0.12	0.88	8273	7471	11450	19582	6562	7000	1.07
S7-3	49135	6602	0.17	0.12	0.86	7850	7204	11600	19728	6230	6800	1.09
S7-4	48876	6601	0.13	0.12	0.89	8983	7913	11719	19513	7061	7300	1.03
S7-5	44609	5455	0.15	0.25	0.77	6321	6176	13037	18861	4745	5200	1.10
S7-6	44379	5406	0.11	0.22	0.83	6986	6609	12837	18385	5509	5200	0.94

$M_n = \min(R_{DSM}M_{ne}, R_{DSM}M_{nl}, M_{nd})$

Table 4.7 Test-to-predicted comparison – all methods

	M_{test}/M_n			
Test #	R-factor	Euro Eq. (10)	Euro Eq. (11)	DSM
S1-1	0.64	0.59	0.69	0.90
S1-2	0.70	0.70	0.76	0.85
S1-3	0.77	0.79	0.86	0.89
S1-4	0.69	0.64	0.73	0.86
S1-5	0.73	0.67	0.77	0.91
S1-6	0.76	0.70	0.79	0.91
S1-7	0.70	0.64	0.73	0.86
S1-8	0.82	0.78	0.89	0.95
S1-9	0.58	0.53	0.61	0.80
S1-10	0.96	0.76	0.90	1.12
S1-11	1.00	0.85	0.94	1.12
S1-12	1.19	0.92	1.07	1.25
S1-13	0.85	0.66	0.77	0.95
S1-14	1.12	1.25	1.25	1.08
S1-15	1.18	1.00	1.00	1.01
S1-16	1.01	0.84	0.84	0.84
S2-1	0.95	0.86	0.86	1.05
S2-2	0.89	0.81	0.81	0.99
S2-3	0.87	0.82	0.90	1.02
S2-4	0.98	0.92	1.01	1.14
S2-5	0.87	0.82	0.89	1.02
S2-6	1.06	0.99	0.99	1.25
S2-7	1.12	1.05	1.05	1.33
S2-8	1.02	0.93	1.05	1.30
S2-9	1.02	0.95	1.06	1.33
S3-1	1.36	1.45	1.50	1.56
S3-2	1.26	1.42	1.42	1.43
S4-1	1.22	1.22	1.25	1.19
S4-2	1.37	1.48	1.48	1.43
S5-1	1.29	1.39	1.43	1.51
S5-2	1.18	1.35	1.35	1.56
S6-1	0.89	0.98	1.03	1.13
S6-2	0.86	0.94	1.00	1.10
S6-3	0.84	0.92	0.98	1.09
S6-4	0.74	0.80	0.86	0.97
S6-5	0.97	1.13	1.16	1.03
S6-6	0.89	1.05	1.06	0.97
S6-7	0.75	0.84	0.90	1.00
S6-8	0.85	0.94	1.00	1.04
S6-9	0.98	0.82	0.91	1.05
S6-10	1.12	0.92	1.01	1.12
S6-11	0.97	0.79	0.90	0.98
S6-12	0.88	1.02	1.02	0.92
S6-13	0.90	1.04	1.04	0.96
S6-14	0.78	0.99	0.99	1.00
S6-15	1.05	1.27	1.27	1.19
S6-16	0.90	1.12	1.12	1.10
S6-17	1.09	1.18	1.18	1.03
S6-18	0.90	0.90	0.93	0.85
S6-19	0.95	0.95	0.98	0.84
S6-20	1.01	1.02	1.04	0.93
S6-21	0.98	0.98	1.01	0.87
S6-22	0.94	0.94	0.98	0.87
S6-23	0.84	0.84	0.87	0.77
S6-24	0.88	0.88	0.91	0.81
S6-25	0.87	0.87	0.90	0.81
S7-1	1.01	0.98	1.02	1.07
S7-2	0.96	0.94	0.99	1.07
S7-3	0.93	0.96	1.00	1.09
S7-4	0.99	0.95	0.98	1.03
S7-5	0.89	0.95	0.95	1.10
S7-6	0.91	0.88	0.88	0.94

4.7 Conclusions

A DSM prediction framework is introduced for through-fastened metal building wall and roof systems and validated for the case of simple span C- and Z-section girts and purlins with compression flanges laterally unbraced. The global, local-global, and distortional buckling capacities are determined with a typical DSM calculation using finite strip eigen-buckling analysis. System effects, i.e., girt or purlin interacting with the through-fastened panel, is simulated in a finite strip eigen-buckling analysis with a rotational spring. Then the global buckling and local-global buckling capacities are reduced to account for the longitudinal stresses that occur at the web-free flange intersection as the girt or purlin deforms from shear flow-induced rotation. The rotation occurs about a center of twist defined by the cross-section shape and the type of through-fastened connection.

A newly assembled database of 62 simple span tests was used to evaluate the DSM and compare its accuracy to the existing Eurocode and AISI R-factor methods. The DSM predictions resulted in the highest LRFD resistance factor because of its slightly conservative test-to-predicted mean and the lowest coefficient of variation among the methods evaluated. Modifications are suggested to the existing Eurocode method to improve its prediction accuracy for Z-sections. The existing AISI S100 R-factor prediction approach for simple spans is unconservative for Z-sections, and improvements are needed in AISI-S100-07 Section D6.1 to reach a goal reliability index of 2.5 for through-fastened metal building wall and roof systems.

Girt and purlin design for wind loads has been a broadly studied research area for over 50 years. This is because purlins and girts play a critical role in metal building

systems, supporting the exterior building shell and provide out-of-plane bracing to the primary moment frames [26]. The research presented herein lays the groundwork for a metal building strength prediction framework employing the DSM that can accommodate gravity loads or wind loads, simple spans and continuous spans, standing seam roofs, and insulated roof and wall systems in the future.

Acknowledgements

The authors are grateful to MBMA and AISI for supporting and guiding this work. We offer a special thanks to Dr. Lee Shoemaker and Dr. Teoman Peköz for sharing their valuable historical perspectives on girt and purlin research. This paper was written with support from an MBMA Faculty Fellowship.

References

[1] Winter G, Lansing W, McCalley RB. Performance of laterally loaded channel beams. Engineering Structures Supplement, Colston Papers 1949; 2, 179-190.
[2] Zetlin L, Winter G. Unsymmetrical bending of beams with and without lateral bracing. ASCE Journal of Structural Division 1955; 81, 774-1.
[3] Vieira LCM, Malite M, Schafer BW. Simplified models for cross-section stress demands on C-section purlins in uplift. Thin-Walled Structures 2010; 48(1), 33-41.
[4] Seely FB, Putnam WJ, Schwalbe WL. The torsional effect of transverse bending loads on channel beams. Engineering Experiment Station 1930; P211, University of Illinois, Urbana.
[5] EN-1993-1-3. Eurocode 3: Design of steel structures. European committee for standardization. Brussels, Belgium; 2006.
[6] Douty RT. A design approach to the strength of laterally unbraced compression flanges. Bulletin No. 37, Cornell University Engineering Experiment Station; 1962.
[7] Peköz T, Soroushian P. Behavior of C- and Z-purlins under wind uplift. *Proc., 6th International Specialty Conference on Cold-Formed Steel Structures*, Rolla, MO; 1982.
[8] Laboube RA. Laterally unsupported purlins subjected to uplift. Report for Metal Building Manufacturers Association, Cleveland, OH;1983.
[9] Rousch CJ, Hancock GJ. Comparison of tests of bridged and unbridged purlins with a non-linear analysis model. Journal of Constructional Steel Research 1997; 41(2-3), 197-220.

[10] LaBoube RA. Roof panel to purlin connections: rotational restraint factor. *Proc., IABSE Colloquium on Thin-Walled Metal Structures in Buildings,* Stockholm, Sweden; 1986.
[11] Rousch CJ, Hancock GJ. Purlin-sheeting connection tests. Research report R724, School of Civil and Mining Engineering, The University of Sydney, Australia; 1996.
[12] AISI S100-07 North American specification for the design of cold-formed steel structural members. American Iron and Steel Institute, Washington, D.C.; 2007; 2007.
[13] AS/NZS-4600. Australian/New Zealand Standard: Cold-formed steel structures; 2005.
[14] Fisher JM. Uplift capacity of simple span Cee and Zee members with through-fastened roof panels. Final report: MBMA 95-01. Metal Building Manufacturers Association, Cleveland, OH; 1996.
[15] Gao T, Moen CD. Flexural strength experiments on exterior metal building wall assemblies with rigid insulation. Journal of Constructional Steel Research 2012. (to appear).
[16] Peköz, Teoman, personal communication, June 6, 2012.
[17] Gao T. Limit state design of metal building roof and wall systems loaded in wind uplift or suction. Ph.D. Dissertation, Virginia Tech, Blacksburg, VA; 2012
[18] Lucas RM, Al-Bermani FGA, Kitipornchai S. Modelling of cold-formed purlin sheeting systems. Part 1: full model. Thin-Walled Structures 1997; 27(3), 223-243.
[19] Gao T, Moen CD. Predicting rotational restraint provided to wall girts and roof purlins by through-fastened metal panels. Thin-Walled Structures 2012 (to appear).
[20] Gao T, Moen CD. Test videos-flexural strength experiments on exterior metal building wall assemblies with rigid insulation. Virginia Tech, Blacksburg, VA. 2012. <http://hdl.handle.net/10919/18714>.
[21] Gao T, Moen CD. Flexural strength of exterior metal building wall assemblies with rigid insulation. Proc., Annual Stability Conference Structural Stability Research Coucil, Grapevine, TX; 2012.
[22] Schafer BW, Adany S. Buckling analysis of cold-formed steel members using CUFSM: conventional and constrained finite strip methods. Proc., 18th International Specialty Conference on Cold-Formed Steel Structures, Orlando, FL; 2006
[23] LaBoube RA, Golovin M. Uplift behavior of purlin systems having discrete braces. Proc., 10th International Specialty Conference on Cold-Formed Steel Structures, Rolla, MO; 1990.
[24] Hancock GJ. Tests of purlins with screw fastened sheeting under wind uplift. Proc., 10th International Specialty Conference on Cold-Formed Steel Structures, Rolla, MO; 1990.
[25] Gao T, Moen CD. Flexural strength of exterior metal building wall assemblies with rigid insulation. Virginia Tech Research Report No. CE/VPI-ST-11/01, Blacksburg, VA, 2011.
[26] Perry DC, McDonald JR, Saffir HS. Performance of metal buildings in high winds. Journal of Wind Engineering and Industrial Aerodynamics 1990; 36(2), 985-999.

Chapter 5: Direct Strength Method for Metal Building Wall and Roof Systems with Rigid Board Insulation - Simple Span Through-Fastened Girts and Purlins with Laterally Unbraced Compression Flanges

*(*Submitted to the *Journal of Constructional Steel Research)*

"Direct Strength Method for Metal Building Wall and Roof Systems with Rigid Board Insulation - Simple Span Through-Fastened Girts and Purlins with Laterally Unbraced Compression Flanges"

Abstract

In this study, the Direct Strength Method (DSM) prediction method for the simple span purlin and girt with one flange through-fastened to the bare panels under uplift and suction loading is extended to the case when the rigid board insulation is added between the purlin (girt) and panels where the rotational restraint provided by the insulation to the purlin (girt) is changed. A simple method is developed to calculate the rotational restraint, and the calculation is validated with tests also conducted in this study. The modification in the new DSM prediction method is to replace the full lateral restraint, provided by the through-fastened bare panel, with the partial lateral restraint due to the thickness of the board. The new DSM prediction is evaluated with 18 full scale tests of wall systems where the insulation is used.

5.1 Introduction

The design for the roof and systems under the uplift and suction wind loading that places the laterally unbraced flange in compression is complicated. The shear flow introduced by the uplift (suction) loading causes the cross-section to rotate, and combines with lateral-torsioal buckling deformation at failure. As for energy efficiency purpose, the rigid board insulation is highly recommended by the energy code, e.g., ASHRAE-90.1 2010 [1]. Recently, equations for calculating the rotational restraint provided by the through-fastened bare panel to the purlin (girt) and DSM method for predicting the flexural capacity of simple span purlin (girt) through-fastened to bare panel were developed by Gao and Moen [2-3]. The objective of this study is to extend the DSM

prediction method to the case when the rigid board insulation is used. The major difference between the cases of with and without rigid board insulation is the lateral restraint provided to the purlin (girt) through the through-fastened flange, i.e. the restraint to the purlin (girt) in the direction parallel to the sheathing. In the case of without insulation, the bare panel provides a full lateral restraint to the through-fastened flange. However, in the case of with insulation, due to the thickness of the board, the sheathing may not provide full lateral restraint to the though-fastened flange. This restraint modification will be applied in the DSM prediction method. A simple method is also developed to calculate the rotational restraint provided by the insulation, and the rotational restraint tests are conducted to validate the calculation. The DSM prediction method for the case with insulation will be evaluated with the experiments, Vacuum box test, conducted by Gao and Moen [4].

5.2 Rotational restraint test

5.2.1 Test setup and procedure

Each specimen was an assembly of 1- 1524mm long C- or Z-section cold-formed steel stud, rigid board insulation (Dow Thermax) strip and 2- 0.46 mm thick 762 mm by 1524 mm panels (see Fig. 5.1). The two panels are joined using 6.4 mm diameter fasteners at the panel edges to form a 1524 mm by 1524 mm panel. The member flange is through-fastened to the panel with #12-14 self drilling screws every 305 mm (adjacent to the rib) with the insulation sandwiched between the girt and panel. The base of each specimen was clamped between 152 mm by 102 mm by 7.9 mm steel angles. The angles have pre-drilled holes every 146 mm and are through-fastened and clamped with 15.8 mm diameter structural bolts. Plaster was poured 152 mm high in the voids between the

angles and the metal panel ribs to prevent crushing of the panel. The web bending and panel bending effects during the test were removed according to the Eq. (9) and (11) in Gao and Moen's study [2].

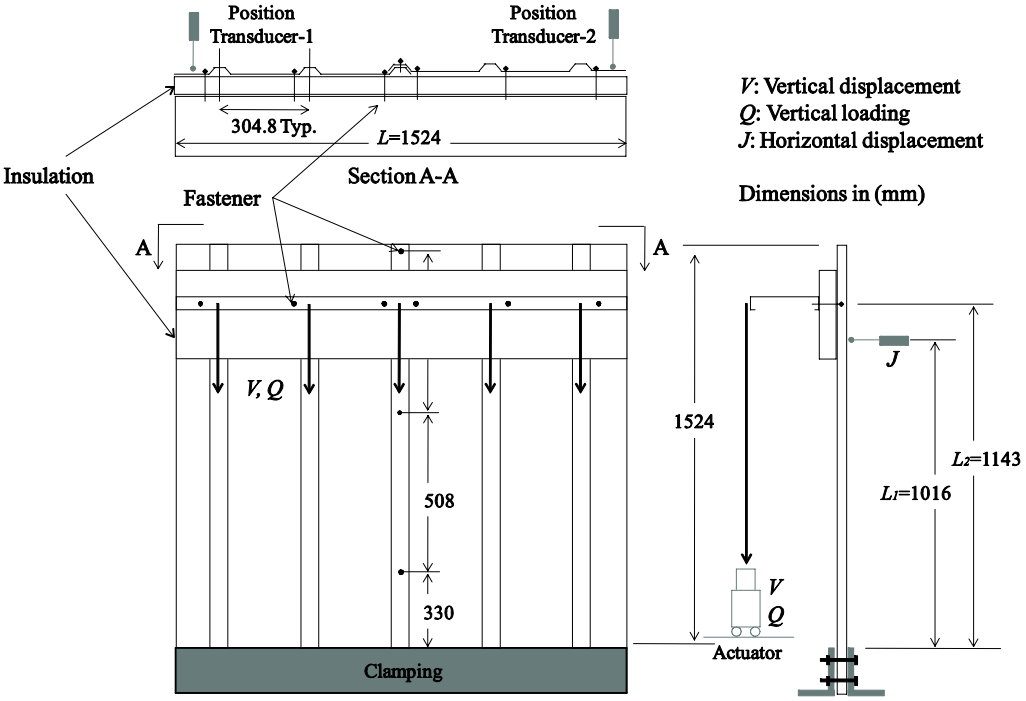

Fig. 5.1 Test setup

5.2.2 Board compression properties

The compressive stress-strain curve of foam was obtained experimentally using 50mm thick foam, and a tri-linear response is observed in Fig. 5.2. The foam deforms linear elastically (stiffness=6.70MPa) until the cell walls buckle and the material loses stiffness (yield stress=0.154 MPa). The stiffness decreases to 0.0689 MPa in the plastic plateau, and increases again after the foam cells have completely collapsed, i.e. hardening behavior.

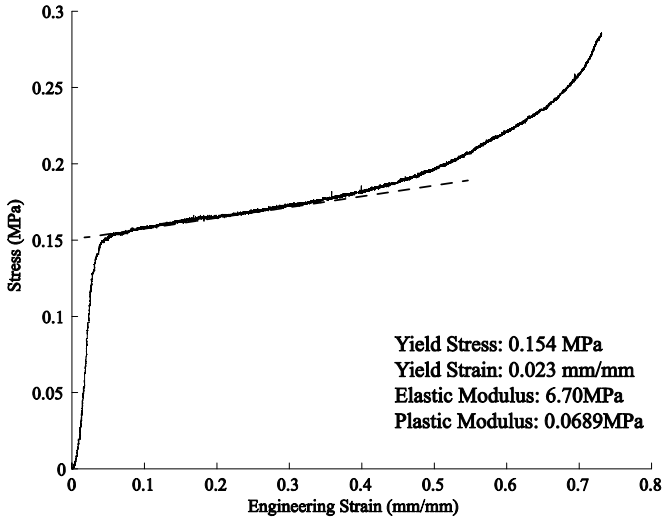

Fig. 5.2 Foam compressive stress-strain curve

5.2.3 Moment-rotation loading response

Eleven specimens were tested (see Table 5.1) and the detailed specimen dimensions and results discussion were reported by Gao and Moen [5]. Under the loading, the through-fastened flange is indented into the foam as shown in Fig. 5.3. A typical load-deformation (moment-rotation) response is shown in Fig. 5.4 for a Z-section, 200mm web and 50mm thick board. Tri-linear behavior is observed, i.e. note initially stiff response, then softer response, then stiffer response, which is consistent with the compressive stress-strain behavior in Fig. 5.2. Since the foam yield stress is very low (F_y=0.154) and the yield strain is only 0.023, it is believed that the demand stress in the foam in a system test, i.e. Vacuum box test, falls in the second linear region (plastic plateau between "o"s) in Fig. 5.4. The stiffness (rotational stiffness) of the second linear region will be used in DSM prediction method and calculated in the next section based on the plastic behavior (second linear region in) obtained from the compressive stress-strain curve (Fig. 5.2). The hardening behavior observed in the rotational restraint test (see Fig.

5.4) is not observed in the system test. The other test's load-deformation responses are summarized in the report by Gao and Moen [5]

Fig. 5.3 Form indentation

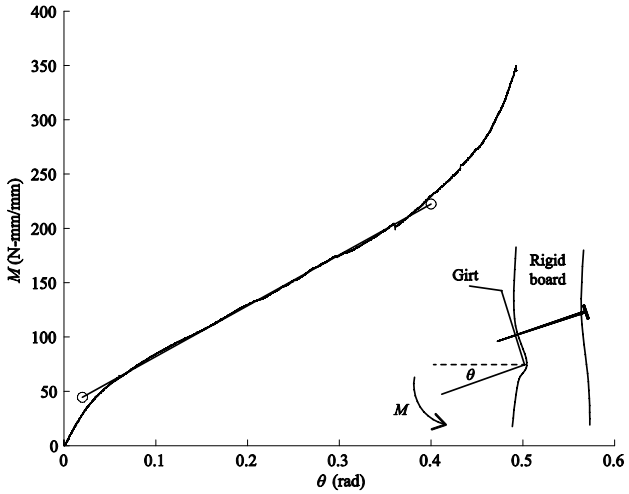

Fig. 5.4 Typical loading curve for Z-section, 200mm web, 50mm board test#2

5.3 Rotational restraint calculation

As shown in Fig. 5.5, the girt rotation θ_1 at a moment M_1 is approximately calculated as:

$$\theta_1 = \frac{\Delta_1}{c} = \frac{\varepsilon_1 T}{c} \quad . \tag{5.1}$$

where ε_1 is a plastic strain, T is the foam thickness, and c is the distance between the fastener and the pivot point . Then, the total force F_1 due to the foam indentation is:

$$F_1 = a_1 \delta_y \,. \tag{5.2}$$

In Eq. (5.2), an elastic-perfectly plastic material is assumed, i.e., the stress in the plastic plateau region is equal to the yield stress of the foam (σ_y=0.154MPa). With the assumption of a_1=2Δ_1 based on the experimental observation (see Fig. 5.3) that θ_1 is close to 45^o, F_1 is calculated as:

$$F_1 = 2\varepsilon_1 T \delta_y \,. \tag{5.3}$$

The distance between the F_1 and the fastener is assumed as c, then:

$$M_1 = 2\delta_y c \cdot \varepsilon_1 T \,. \tag{5.4}$$

The girt rotation θ_2 at the moment M_2 can be calculated is the same way with Eq. (5.1) and (5.4), then the rotational restraint is

$$k_\phi = \frac{M_1 - M_2}{\theta_1 - \theta_2} = \frac{2\delta_y c\left(\varepsilon_1 T - \varepsilon_2 T\right)}{\frac{1}{c}\left(\varepsilon_1 T - \varepsilon_2 T\right)} = 2\delta_y c^2 \,. \tag{5.5}$$

This simple equation shows that the k_ϕ is determined by the foam's yield stress normally reported by the insulation manufacturer and the fastener location c. The square relationship between c and k_ϕ is consistent with the study about the rotational restraint provided by the bare metal panel [2].

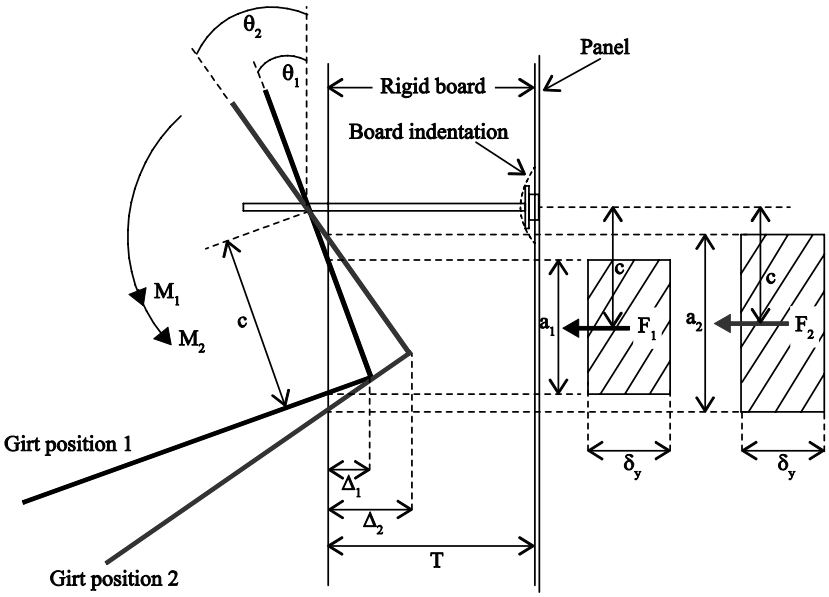

Fig. 5.5 Rotational restraint calculation illustration

The prediction with Eq. (5.5) is compared with the experimental results, i.e. the stiffness visually determined between the two "o" points in a loading curve (see Fig. 5.4) in Table 5.1. The predicted is about 10% conservative with a COV of 22.6%.

Table 5.1 Prediction comparison

Girt profile	Web depth (mm)	Foam thickness (mm)	Series#	k_ϕ Test (N-mm/rad/mm)	k_ϕ Predicted (N-mm/rad/mm)	Test/Predicted
Z	200	25	1	364	367	0.99
Z	200	25	2	337	391	0.86
Z	200	50	1	432	324	1.33
Z	200	50	2	468	397	1.18
C	200	50	1	378	389	0.97
C	100	50	2	367	345	1.06
C	250	50	1	412	428	0.96
C	250	50	2	423	500	0.85
C	150	50	1	243	275	0.88
Z	200	100	1	643	470	1.37
Z	200	100	2	583	361	1.62
					MEAN=	1.10
					COV%=	0.23

The prediction Eq. (5.5) is also conservatively applicable to other rigid board insulation, e.g., XPS insulation. The rotational restraint test of XPS insulation is summarized in Gao and Moen [3].

5.4 DSM prediction for the case with rigid board insulation

The interaction equation for the DSM prediction method is

$$\frac{M}{S_c}+\sigma_f \le \frac{M_{ne}}{S_c} \quad , \quad \frac{M}{S_c}+\sigma_f \le \frac{M_{n\ell}}{S_c} \quad , \tag{5.6}$$

where M is the required flexural strength, S_c is the gross strong centroidal axis section modulus for the extreme compression fiber, and σ_f is the flange bending stress due to free flange deformation [3]. Developed from the interaction equation, the flexural capacity is calculated as M_n=min($R_{DSM}M_{ne}$, $R_{DSM}M_n$, M_{nd}), where M_{ne}, M_n and M_{nd} are the DSM flexural strengths calculated with the elastic buckling strengths, M_{cre} (global buckling), M_{cr} (local buckling) and M_{crd} (distortional buckling), and R_{DSM} is calculated as:

$$R_{DSM} = \left(1+\frac{S_c}{S_f}k_H k_R\right)^{-1} . \tag{5.7}$$

For predicting the case when the rigid board insulation is used, use the same S_c, S_f and k_H as defined in Gao and Moen [3]. However, the reduction factor accounting for the effect of elastic foundation k_R needs to be modified because that the insulation may not provide full lateral restraint. Similar to [3],

$$k_R = \frac{1-0.0225r}{1+1.013r} , \tag{5.8}$$

where

$$r = \frac{KL^4}{\pi^4 EI_f} \tag{5.9}$$

Different from [3], K is calculated as shown in Fig. 5.6,

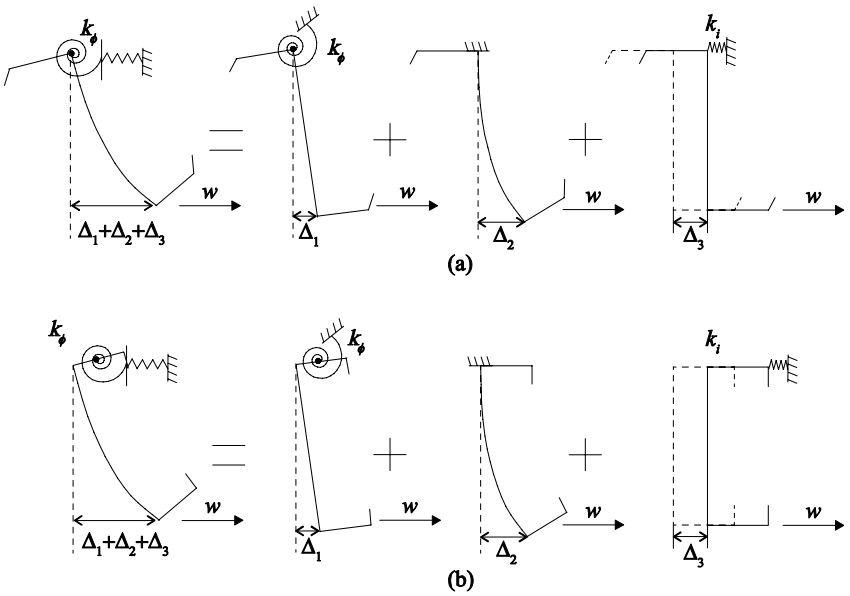

Fig. 5.6 Spring calculation for (a) Z-section and (b) C-section

The equation for *K* is:

$$K = \frac{w}{\Delta_1 + \Delta_2 + \Delta_3} \tag{5.10}$$

where

$$\Delta_1 = \frac{wH}{k_\phi} \cdot H \tag{5.11}$$

and

$$\Delta_2 = \frac{wH^3}{3EI} \quad . \tag{5.12}$$

and

$$\Delta_3 = \frac{w}{k_i} \quad . \tag{5.13}$$

where k_ϕ is calculated with Eq. (5.5). The linear spring k_i represents the partial lateral restraint provided by the insulation, and is approximated at 0.0072N/mm/mm (1 lb/in./in.).

When calculating M_{ne} and M_n from M_{cre} and M_{cr} using finite strip eigen-buckling analysis [6] a rotational spring (k_ϕ) and a linear spring (k_i) are applied at the cross-section's center of twist (see Fig. 5.7a) to simulate the restraint provided by the insulation. The reference stress in the finite strip analysis is calculated assuming restrained bending about the strong centroidal axis as shown in Fig. 5.7b. The critical elastic global buckling moment M_{cre} is multiplied by a moment gradient factor C_b=1.13 to account for the parabolic moment diagram in a simple span.

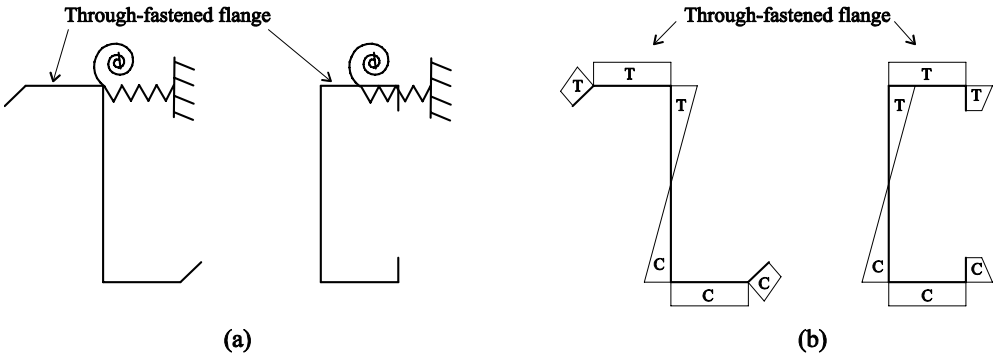

Fig. 5.7 CUFSM analysis (a) spring (b) conference stress

5.5. Results comparison

Eighteen tests with girt failure are used to evaluate the proposed DSM prediction method. The test name (see Table 5.2) are the same as used in Gao and Moen [4], and the detailed cross-section dimension and test parameters can be found. The rotational restraint k_ϕ is calculated with Eq. (5.5). The resistance factor (ϕ) is calculated with AISI-S100 Chapter F [6] (ϕ=2.5).

The prediction is conservative (MEAN=1.07) with coefficient of variation (COV) of 0.19. The resistance factor (ϕ) is 0.91, higher than ϕ=0.9 current specified in AISI-S100-07 for flexural members.

Table 5.2 Test-to predicted comparison

Test name	Girt profile	Web depth (mm)	Girt thickness (mm)	Foam thickness (mm)	M_{test}/M_n
Z200D-TH100-1	Z	203	2.57	100	0.78
Z200D-TH100-2	Z	203	2.59	100	1.02
Z200B-TH100-1	Z	203	2.57	100	0.95
C200D-TH100-1	C	203	2.57	100	0.83
Z250D-TH25-1	Z	254	1.52	25	1.34
Z250D-TH25-2	Z	254	1.52	25	1.01
Z250B-TH25-1	Z	254	1.52	25	1.27
Z250B-TH25-2	Z	254	1.52	25	1.32
C250D-TH25-1	C	254	1.52	25	0.92
C250D-TH25-2	C	254	1.52	25	1.16
Z250D-TH50-1	Z	254	1.52	50	1.06
Z250D-TH50-2	Z	254	1.52	50	1.11
Z250B-TH50-1	Z	254	1.52	50	1.38
Z250B-TH50-2	Z	254	1.52	50	1.30
C250D-TH50-1	C	254	1.52	50	0.89
C250D-TH50-2	C	254	1.52	50	0.67
Z250D-TH100-1	Z	254	1.52	100	1.17
Z250D-TH100-2	Z	254	1.52	100	1.16
Z250B-TH100-1	Z	254	1.52	100	0.96
Z250B-TH100-2	Z	254	1.52	100	1.29
C250D-TH100-1	C	254	1.52	100	0.82
C250D-TH100-2	C	254	1.52	100	1.04
				MEAN=	1.07
				COV=	0.19
				ϕ =	0.91

5.6. Conclusion

In this study, the DSM prediction method for the bare panel roof and wall systems under the uplift and suction loading is extended to predict the case when the rigid board insulation is used. A simple method is proposed to calculate the rotational restraint provided by the insulation and used in the DSM prediction method. A linear spring is used to simulate the partial lateral restraint provided by the insulation. The new DSM method shows a good prediction to the experimental results.

References

[1] ASHRAE-90.1. ASHRAE Standard: Energy Standard for Buildings Except Low-Rise Residential Buildings. American Society of Heating, Refrigerating and Air-Conditioning Engineers, Inc., Atlanta, GA; 2010.
[2] Gao T, Moen CD. Predicting rotational restraint provided to wall girts and roof purlins by through-fastened metal panels. Thin-Walled Structures 2012 (to appear).
[3] Gao T, Moen CD. Metal building wall and roof system design using the Direct Strength Method-through-fastened simple span girts and purlins with laterally unbraced compression flanges. ASCE-Journal of Structural Engineering 2012 (to appear).
[4] Gao T, Moen CD. Flexural strength experiments on exterior metal building wall assemblies with rigid insulation. Journal of Constructional Steel Research 2012. (to appear).
[5] Gao T, Moen CD. Flexural strength of exterior metal building wall assemblies with rigid insulation. Virginia Tech Research Report No. CE/VPI-ST-11/01, Blacksburg, VA, 2011.
[6] AISI-S100. North American Specification for the Design of Cold-Formed Steel Structural Members. Washington, D.C.: American Iron and Steel Institute; 2007.

Chapter 6: Conclusions

6.1 Direct Strength Method prediction

The first objective of this thesis was to develop a Direct Strength Method prediction method for through-fastened purlin and girts under the uplift and suction loading that places the lateral unbraced flange in compression. The non-linear complexity of this problem is caused by the rotation of the purlin or girt cross-section, i.e., the lateral deformation of the free flange, due to the shear flow. This thesis starts with a development of mechanics-based expressions for calculating the rotational restraint provided by a through-fastened bare metal panel. In the calculation, finite element analysis was used to obtain the panel pull-out stiffness, and the flange bending effect was also included. The rotational restraint calculation was then applied in the existing prediction methods, Eurocode and DSM methods, to predict the flexural capacity of through-fastened purlin and girts, and in DSM method, a knock down factor is proposed to account for the capacity reduction due to the lateral deformation of the free flange. The prediction methods, Eurocode, DSM and experimental based R-factor method, were evaluated with 62 through-fastened simple span vacuum box tests assembled by the author. The results showed that DSM prediction method with the proposed knock down factor is overall as accurate as the Eurocode and more accurate than the R-factor method, and the Eurocode prediction for the Z-sections can be easily improved with minor modifications. It is also found that the Eurocode and R-factor predictions are unconservative for Z-sections.

6.2 Metal building wall and roof systems with rigid board insulation

As the second objective of this thesis, vacuum box tests were conducted to investigate the effect of rigid board insulation on through-fastened roof and wall systems

and to determine the R-factors when the rigid board insulation is used. Four failure modes limiting system capacity were observed: panel flexural failure, panel pull-over failure, screw fracture and/or plastic bending and purlin (girt) failure. The controlling limit state is influenced by purlin or girt cross-section slenderness. The failure of a slender cross-section is dominated by member local deformation, and the failure occurs in the member, i.e., purlin (girt) failure. The failure of a stocky cross-section mostly occurs in the through-fastened connection. The failure mode is panel pull-over (without rigid board) and screw failure (with rigid board). For stocky cross-sections, even if the connection does not fail and the failure mode is purlin (girt) failure, the capacity is still reduced by the rigid board insulation because of the lower rotational restraint provided by the rigid board. The results also show that the system capacity is sensitive to the fastener location on the flange, because the rotational restraint is sensitive to the fastener location. The low rotational restraint due to using the rigid board insulation is because of the low insulation yield stress and the plastic region in the insulation board compression stress-strain curve, which also causes a creeping behavior in the vacuum box test where the cross-section continues to rotate at a constant loading pressure.

6.3 Future research

6.3.1. Panel pull-out stiffness in the rotational restraint calculation

It will help the wide implementation of the DSM prediction methods proposed in this thesis if the panel stiffness in the rotational restraint prediction can be calculated with simplified equations or spreadsheet rather than finite element analysis. A preliminary study shows that the large deformation theory of thin-plate bending could be used for the panel stiffness calculation.

6.3.2. The sensitivity of system capacity to the fastener location

It has been shown that the rotational restraint and the system capacity are both sensitive to the fastener location on the flange. So, a statistical study focused on the sensitivity of the system capacity to the fastener location may help the industry understand the importance of the fastener location.

6.3.3. A limit state design for metal building roof (wall) system under uplift (suction) loading

Four different failure modes were observed in Chapter 3: panel flexural failure, panel pull over failure, fastener fracture and/or plastic bending and purlin (girt) failure. So, it is necessary to develop a limit state design for roof (wall) system design under uplift (suction) loading, in which all limit states should be checked.

Panel flexural failure

This failure modes can be easily checked with DSM method in AISI by calculating the flexural strength of the panel at the midspan of purlins (girts).

Panel pull over failure

When the bare panel is used, the panel pull over failure mode needs to be checked. The axial force in the fastener (pulling force) can be calculated as shown in Fig 6.1. The failure of the panel can be predicted with equations in AISI S100-07 E4.4. In Fig 6.1, the q represents the uplift (suction) loading and the shear flow in the web, s is the shear flow in the flange, and n is the bearing force due to the cross-section rotation and calculated based on q and s. The total axial force in the fastener is $n+q$. Notice that for the Z-section (Fig 6.1a), there is also a shear force ($2s$) applied on the panel from the fastener.

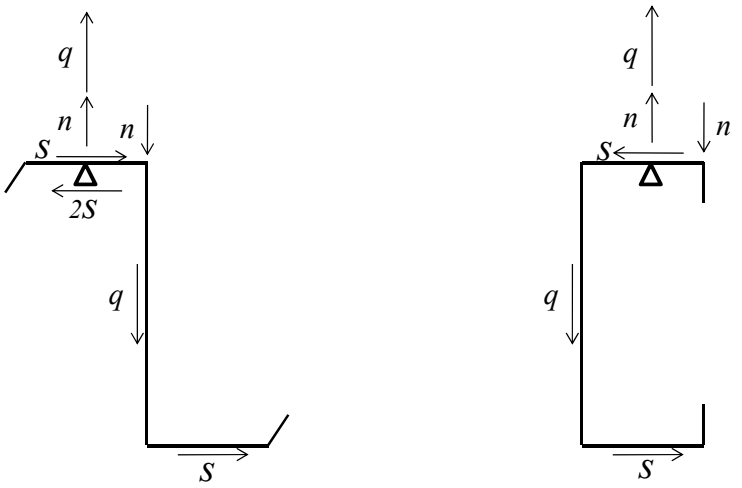

Fig. 6.1 Panel pull over calculation (a) Z-section (b) C-section

Fastener fracture and/or plastic bending

When rigid board insulation is used, the fastener failure due to the concentrated bending moment from the flange needs to be checked. Similar but different from the panel pull-over failure calculation, we assume there is no bearing force developed by the board compression, i.e., the force couple *n* is replaced with a concentrated moment *m* on the fastener. So, the fastener is loaded with an axial force *q*, bending moment *m* and a shear force *2s* for Z-section. Notice that the flange has to be thick enough in order to clamp the fastener and apply the concentrated bending moment *m*. So, the minimum flange thickness that can clamp the fastener needs to be determined possibly by experiments.

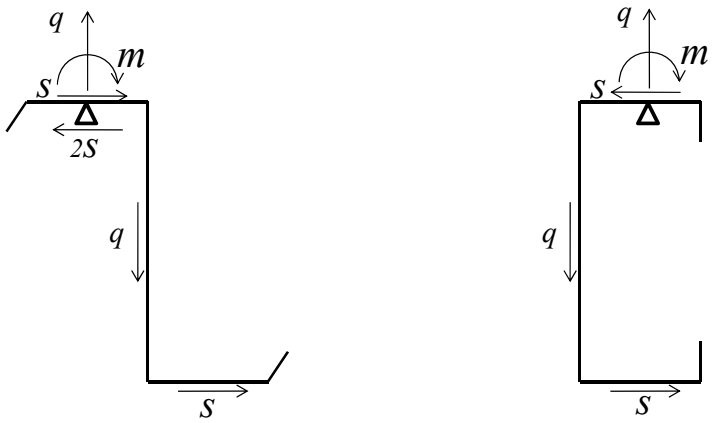

(a) (b)

Fig. 6.2 Fastener failure (a) Z-section (b) C-section

Purlin (girt) failure

The purlin (girt) failure prediction has been discussed in this thesis.

6.3.4. Extension to continuous span, gravity (pressure) loading and standing seam roof design

To expand the Direct Strength Method approached presented herein from simple spans to the continuous spans under wind uplift or suction, the member capacity in the negative moment region needs to be checked. For the bare panel case, the negative moment region is assumed to be fully braced by the panel and the primary frame's flange. But for the case when the rigid board insulation is used, lateral restraint provided to the through-fastened flange may be reduced due to the board thickness, and the reduction of the lateral restraint should be quantified experimentally in the future. In this case, the span in the negative moment region is not fully braced anymore. This reduction of lateral restraint is also important for the design of gravity (pressure) loading that places the through-fastened flange in compression. For the bare panel case, the cross-section is

assumed to be fully braced if the free flange is in tension and the through-fastened flange is in compression, but it may not be the case when the rigid board is sandwiched between the through-fastened flange and the bare panel.

To expand the prediction method for through-fastened system to the standing seam roof, it may only need to replace the restraints, i.e., lateral restraint and rotational restraint, provided by the through-fastened system to those provided by the sanding seam roof.

End
August 03, 2012
Tian Gao